Joint Propulsion Conferences
July 14 - 17, 2013, San Jose, CA
49th AIAA/ASME/SAE/ASEE Joint Propulsion Conference

Mode Transitions in Hall Effect Thrusters

Michael J. Sekerak[*], Benjamin W. Longmier[†] and Alec D. Gallimore[‡]
University of Michigan, Ann Arbor, MI, 48109

Daniel L. Brown[§]
U.S. Air Force Research Laboratory, Edwards Air Force Base, California 93524

and

Richard R. Hofer[**] and James E. Polk[††]
Jet Propulsion Laboratory, California Institute of Technology, Pasadena, CA 91109

Mode transitions have been commonly observed in Hall Effect Thruster (HET) operation where a small change in a thruster operating parameter such as discharge voltage, magnetic field or mass flow rate causes the thruster discharge current mean value and oscillation amplitude to increase significantly. Mode transitions in a 6-kW-class HET called the H6 are induced by varying the magnetic field intensity while holding all other operating parameters constant and measurements are acquired with ion saturation probes and ultra-fast imaging. Global and local oscillation modes are identified. In the global mode, the entire discharge channel oscillates in unison and azimuthal perturbations (spokes) are either absent or negligible. Downstream azimuthally spaced probes show no signal delay between each other and are very well correlated to the discharge current signal. In the local mode, signals from the azimuthally spaced probes exhibit a clear delay indicating the passage of "spokes" and are not well correlated to the discharge current. These spokes are localized oscillations propagating in the E×B direction that are typically 10-20% of the mean value. In contrast, the oscillations in the global mode can be 100% of the mean value. The transition between global and local modes occurs at higher relative magnetic field strengths for higher mass flow rates or higher discharge voltages. The thrust is constant through mode transition but the thrust-to-power decreased by 25% due to increasing discharge current. The plume shows significant differences between modes with the global mode significantly brighter in the channel and the near-field plasma plume as well as exhibiting a luminous spike on thruster centerline. Mode transitions provide valuable insight to thruster operation and suggest improved methods for thruster performance characterization.

[*] Doctoral Candidate, Plasmadynamics and Electric Propulsion Laboratory, Department of Aerospace Engineering, 1919 Green Road, B107, Ann Arbor, MI 48105, msekerak@umich.edu, Member AIAA.
[†] Assistant Professor, Plasmadynamics and Electric Propulsion Laboratory, Department of Aerospace Engineering, 1320 Beal Avenue, Ann Arbor, MI, 48109, longmier@umich.edu, Member AIAA.
[‡] Arthur F. Thurnau Professor and Director, Plasmadynamics and Electric Propulsion Laboratory, Department of Aerospace Engineering, College of Engineering, 1320 Beal Avenue, Ann Arbor, MI, 48109, alec.gallimore@umich.edu, Fellow AIAA.
[§] Research Scientist, Aerospace Systems Directorate, In-Space Propulsion Branch, Air Force Research Laboratory, 1 Ara Rd, Edwards AFB, CA, daniel.brown@edwards.af.mil, Member AIAA.
[**] Senior Engineer, Electric Propulsion Group, 4800 Oak Grove Dr., MS 125-109, Pasadena, CA, 91109, richard.r.hofer@jpl.nasa.gov, Associate Fellow AIAA.
[††] Principal Engineer; Propulsion and Materials Engineering Section, 4800 Oak Grove Dr., MS 125-109, Pasadena, CA, 91109, james.e.polk@jpl.nasa.gov, Associate Fellow AIAA.

Nomenclature

A_b = area of discharge channel bin, cm^2
A_{chnl} = area of discharge channel, cm^2
A_p = probe area m^2
$a(b,t)$ = average pixel value per bin
B_r = peak radial magnetic field, G
B_r^* = nominal peak radial magnetic field, G
B_r / B_r^* = normalized peak radial magnetic field
b = bin number
c_1 = linear fit coefficient (m_0 to I_D)
c_2 = linear fit coefficient (m_0 to I_D)
D = diffusion coefficient, $m^2\ s^{-1}$
$D_\perp$ = cross-field diffusion coefficient, $m^2\ s^{-1}$
E_z = axial electric field, $V\ m^{-1}$
E_θ = azimuthal electric field, $V\ m^{-1}$
e = elementary charge, 1.60×10^{-19}, C
f = frequency, s^{-1}
I_B = magnet coil current, A
$I_D(t)$ = discharge current, A
$\overline{I}_D$ = mean discharge current, A
$\hat{I}_D(t)$ = normalized, AC component of the discharge current
$I_{D_{AC}}(t)$ = AC component of the discharge discharge current, A
I_{IM} = inner magnet coil current, A
I_{ISR} = ion saturation reference current, A
I_{OM} = outer magnet coil current, A
$J_{D_b}(f,\gamma)$ = 2-D discrete Fourier transform of j_{D_b}
$j_D(t)$ = discharge current density, $mA\ cm^{-2}$
$j_{D_b}(t)$ = discharge current density per bin, $mA\ cm^{-2}$
$\overline{j}_D$ = average discharge current density, $mA\ cm^{-2}$
k_b = Boltzmann's constant, 1.38×10^{-23}, $J\ K^{-1}$
k_m = rate coefficient for electron-neutral collisions, $m^3\ s^{-1}$
k_θ = azimuthal wave number, $rad\ m^{-1}$
L_{chnl} = channel length, m
M_b = number of pixels per bin
m = spoke order
m_0 = spoke order $m = 0$
m_e = electron mass, 9.11×10^{-31} kg
m_i = Xe ion mass, 2.18×10^{-25}, kg
$\dot{m}_a$ = anode mass flow rate, $mg\ s^{-1}$
$\dot{m}_c$ = cathode mass flow rate, $mg\ s^{-1}$
N = neutral density, m^{-3}
N_f = number of frames
N_b = number of bins
n_e = electron density, m^{-3}
n_i = ion density, m^{-3}
PSD_{1D} = 1-D power spectral density, Arb Hz^{-1}
PSD_{2D} = 2-D power spectral density, Arb Hz^{-1}
$p(x,y,t)$ = pixel value
$\tilde{p}(x,y,t)$ = AC coupled pixel value
$\overline{p}(x,y)$ = mean pixel value
R_{xy} = cross-correlation between x and y
r = mean channel radius, m
r_o = outer channel radius, cm
r_i = inner channel radius, cm
S_N = periodogram spectral estimate, Arb Hz^{-1}
T_e = electron temperature
$T_{e\square}$ = electron temperature parallel to magnetic field, eV
$T_{e\perp}$ = electron temperature perpendicular to magnetic field, eV
V_D = discharge voltage, V
V_f = floating potential, V
V_p = plasma potential, V
v_{z-eff} = effective cross-field velocity, $m\ s^{-1}$
v_{ph} = phase velocity, m/s
$X(f)$ = discrete Fourier transform of $x(t)$
β = rate coefficient for electron-ion collisions, $m^3\ s^{-1}$
γ = inverse angle from 2D DFT, deg^{-1}
$\overline{\varepsilon}$ = mean electron energy, eV
ε^* = material dependent cross-over energy, eV
Λ = plasma parameter
μ = mobility coefficient, $C\ s\ kg^{-1}$
$\mu_\perp$ = cross-field mobility coefficient, $C\ s\ kg^{-1}$
ν_{eff} = effective collision frequency, s^{-1}
ν_{e-N} = electron-neutral collision frequency, s^{-1}

ν_{e-i} = electron-ion collision frequency, s^{-1}
ρ_{xy} = linear correlation coefficient between signals x and y
$\bar{\sigma}$ = effective total secondary electron emission yield
$\sigma_a(b,t)$ = uncertainty in a for bin b
$\sigma_{j_{D_b}}(b,t)$ = uncertainty in discharge current density for bin b, mA cm^{-2}
$\Delta\Phi_s$ = plasma sheath potential, V
ω = frequency, rad s^{-1}
ω_c = electron cyclotron frequency, rad s^{-1}

I. Introduction

HALL Effect Thrusters (HETs) have been under development since the 1960's, first flew in the 1970's,[1] and are increasingly used for and considered for a variety of space missions, ranging from satellite station-keeping to interplanetary exploration. Despite the extensive heritage of HETs, the physics of their operation is not fully understood as illustrated by inconsistencies in anomalous electron transport experiment and theory, whereby an unexplained excess of electrons cross magnetic fields lines above that predicted by classical diffusion[2] or Bohm diffusion[3]. Understanding the underlying physics of HET operation is important for many reasons including the ability to create first-principles predictive models. These models would enable rapid design iterations not possible currently and would reduce developmental costs because all existing simulations to calculate thruster performance are non-predictive and require empirical factors to match results from real thrusters. Additionally, labor and capital intensive life testing and flight qualification programs could be reduced in cost and augmented with accurate, predictive physics-based simulations. Fully understanding HET physics would ensure that ground testing adequately predicts thruster operation in space where the ambient pressures and local gas density are orders of magnitude lower than in vacuum chambers. Finally, improved models would facilitate the scaling of HETs to very high power and ensure that new designs for the recently developed magnetically shielded[4] or low/zero-erosion concepts are stable across a broad operating range.

Although electron transport is not well understood in HETs, it has been noted to change significantly between different operating modes at similar thruster operating conditions. Plasma oscillations play an integral part in mode transitions, so investigating how the plasma oscillations change during mode transitions will provide insight into anomalous electron transport. While thruster performance and stability are linked to understanding plasma oscillations and the characteristics of HET operating modes, little work has been done to define these operating modes and to quantitatively determine their influence on plasma oscillations as will be shown in this work. This investigation induces mode transitions by varying magnetic field strength in a well characterized 6-kW class HET called the H6 and investigates oscillations with probes and high-speed imaging.

II. Modes and Transitions

HETs have been under development for over 50 years in Russia with significant experimental and flight histories[1] and mode transitions have been commonly observed throughout their development as noted by some of the early pioneering Russian research.[5] HETs have several parameters that define a single operating point such as discharge voltage, magnetic field strength (or magnet coil current), anode mass flow rate and cathode mass flow rate. Laboratory HET discharge power supplies operate in voltage regulated mode where the discharge voltage between the anode and cathode is held constant and the discharge current is allowed to fluctuate. A general, qualitative description of mode transition can be deduced from previous research as the point while varying one parameter and maintaining all others constant, a sharp discontinuity is observed in the discharge current mean and oscillation amplitude. In one mode, the discharge current oscillation amplitude is small with respect to the mean discharge current value, while after the mode transition the mean discharge current rises sharply as well as the oscillation amplitude. Two ideas may play a role in mode transitions. The first idea involves wall effects and has been proposed with accompanying physical mechanism and modeling. The second idea involves more recent investigations that suggest the plume physics in the region immediately downstream of the discharge channel exit (near-field plume) has an influence on mode transitions, although the physical mechanisms were beyond the scope of study. While the answer is likely a combination of the two ideas (and possibly other ideas not yet proposed),

investigating the plasma oscillations during mode transition offer insight into the underlying mechanisms. This investigation only considers magnetic layer thrusters with deep discharge channels and non-conducting walls, but anode layer thrusters have exhibited similar mode transitions[6] to those described below.

A. Mode Transition in the SPT-100 due to Wall Effects and Space Charge Saturation

Gascon[7] investigated different wall material effects on SPT-100 thruster operation including borosil (BN-SiO_2), alumina (Al_2O_3), silicon carbide (SiC) and graphite (C). The significant differences being ion bombardment sputter yield and secondary electron emission yield coefficients as well as conductivity in the case of graphite. Here we only discuss the borosil results as the closest to the Boron Nitride (BN) used in the H6. Varying the magnetic field by changing the magnetic coil current (I_B) as shown in Figure 1 results in a sharp mode transition between 3.5 and 4.0 A. Below the magnetic field transition threshold the mean discharge current (I_D) and discharge current oscillation amplitudes increase significantly. This work was related to a previous study by Gascon[8] where azimuthally spaced probes were used to investigate wave propagation and mode transitions were also observed.

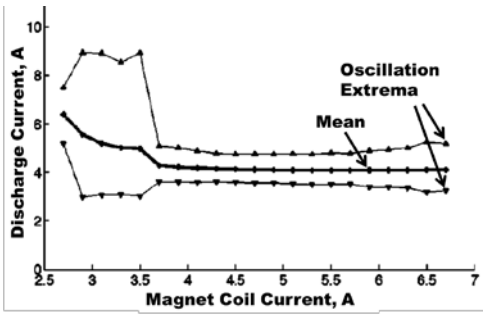

Figure 1. SPT-100 mean discharge current (crosses) and oscillation extrema (triangles) for anode flow rate of 5 mg/s and 300-V dishcarge voltage with variable magnetic field strengh represented by magnetic coil current. Reproduced from Figure 2 of Ref. 7 for borasil.

In a companion paper to Gascon's later work, Barral[9] expanded on the ideas of Baitin[10] and Jolivet and Roussel[11] who considered the effect of secondary electron emission on sheath potentials in HETs. A 1-D axial fluid model was developed that accounts for electron temperature anisotropy with different electron temperatures along $(T_{e\parallel})$ and perpendicular $(T_{e\perp})$ to magnetic field lines. The sheath potential, $\Delta\Phi_S$, from balancing ion and electron flux to the wall with effective total secondary electron emission yield, $\bar{\sigma}$, is

$$\Delta\Phi_S = \frac{k_B T_{e\parallel}}{e} \ln\left[\left(1-\bar{\sigma}\right)\sqrt{\frac{m_i}{2\pi m_e}}\right] \tag{1}$$

where m_i is the ion mass, m_e is the electron mass, e is the elementary charge and k_b is Boltzmann's constant. Once $\bar{\sigma}$ approaches unity, Eq. (1) results in a singularity and the sheath becomes space charge saturated (SCS) where the potential is no longer monotonically changing. This results in a potential well that traps electrons near the wall as shown in Figure 2. The mean energy of electrons at the wall ($\bar{\varepsilon}$), which is a function of $T_{e\parallel}$ and $T_{e\perp}$, determines $\bar{\sigma}$ and was based on a linear fit to experimental data.

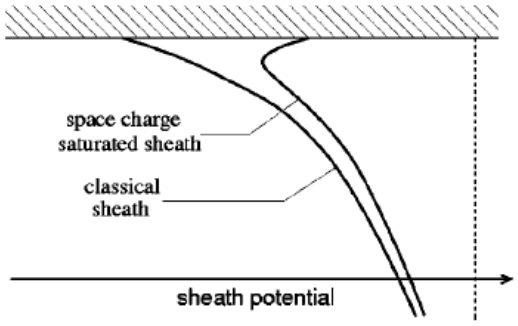

Figure 2. Sheath potential profiles at the wall with and without SCS. Reproduced from Figure 3 of Ref. 9.

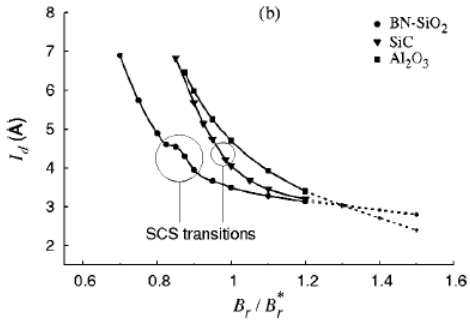

Figure 3. Simulated discharge current from 1-D fluid model with magnetic field variations for different wall materials. B_r is the maximum radial magnetic field and B_r^* is the nominal value. The steep rise in discharge current is attributed to the space charge saturation transition. Reproduced from Figure 10(b) of Ref. 9.

The classical cross-field mobility for electron transport is used in the 1-D model so no adjustable parameters to account for anomalous electron transport are used to fit experimental data.[9] Therefore, the simulation results can only be qualitatively compared to experimental results. When the mean electron energy at the wall $\bar{\varepsilon}$ (a function of $T_{e\parallel}$ and $T_{e\perp}$) for a given axial position in the discharge channel exceeds a material dependent crossover energy $\left(\bar{\varepsilon} > \varepsilon^*\right)$, then $\bar{\sigma} \to 1$ and that position on the discharge channel wall is in SCS. As discharge voltage increases and more energy is available to increase $T_{e\parallel}$ and $T_{e\perp}$, or as magnetic field strength decreases and energy is more easily transferred across magnetic field lines, $\bar{\sigma}$ increases and more of the channel length is in SCS. The SCS regime starts at the maximum radial magnetic field strength location where the electron temperature is highest, which is at the exit plane for the SPT-100, and migrates upstream in the discharge channel towards the anode as thruster operating conditions change; i.e. discharge voltage and magnet coil current.

The implication is the potential well near the wall surface for regions in SCS provides the electrons an easier path across magnetic field lines, also known as near-wall conductivity. As the SCS region grows along the channel length, the low impedance path eventually reaches a region of lower magnetic field (increased mobility) or where the magnetic field lines are parallel to the wall and the electrons can easily reach the anode, resulting in a significant increase in discharge current. The magnetic field lines for the SPT-100B are shown in Figure 4. Note the magnetic field lines intersect the wall perpendicularly (almost purely radial in direction) at the exit plane in the location of maximum radial magnetic field, but the magnetic fields have a large axial component (parallel to the wall) farther into the discharge channel where the field is weaker. The model used in Ref. 9 is 1-D (axial) and only considers a radial magnetic field, while Figure 4 clearly shows the magnetic field has significant axial and radial components upstream from the exit plane. The qualitative shape of the transition between high-current to low-current is captured by the model and SCS theory as shown by comparing Figure 1 to Figure 3, however the quantitative magnitudes differ without empirical coefficients for electron transport.

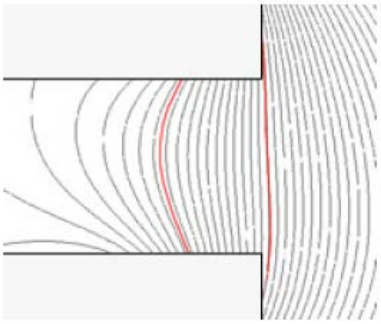

Figure 4. SPT-100B magnetic field lines. Reproduced from Figure 2a of Ref. 12.

B. Low Voltage Operation of the H6 and Azimuthal Spokes

Brown[13] showed that at low discharge voltages (100-120 V), the H6 thruster would operate either at a high-efficiency "low-current" mode with low mean discharge current values and low-amplitude oscillations, or low-efficiency "high-current" mode with high mean discharge current values and strong oscillations. It is important to note that the transition between modes occurred by making slight changes in either magnetic field settings, background vacuum chamber pressure, or cathode flow rate, or by introducing ambient gas near the center-mounted cathode. Varying discharge voltage for various cathode flow fractions (CFF)* in Figure 5 showed the discharge current decreased by approximately 10% when transitioning from "high-current" to "low-current" mode. Figure 5 also shows the transition occurs at higher discharge voltage for lower CFF. From Figure 13 of Ref. 13 the discharge current PSD decreased by over two orders of magnitude when transitioning from the "high-current" mode

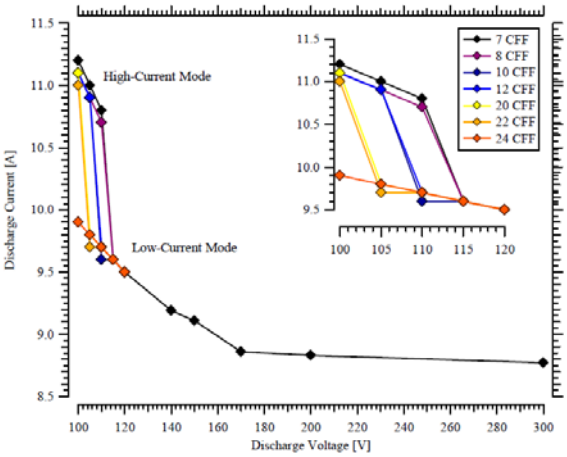

Figure 5. Change in discharge current between high-current mode and low-current mode for the H6 at low voltages. Reproduced from Figure 9 of Ref. 13.

* Cathode flow fraction is the mass flow rate of gas through the cathode divided by the mass flow rate of gas through the anode.

to the "low-current" mode. Note that for this study, the magnetic field was varied in order to maximize thruster efficiency. This transition occurred at higher voltages (closer to flight levels) and at lower chamber pressure, suggesting that the thrusters may operate differently in the space environment than in test facilities on Earth. During the transition from "high-current" to "low-current" modes, the thrust remained constant, but the decreased discharge current resulted in up to a 20% increase in thrust-to-power. Using an array of plume diagnostics including a nude Faraday probe, retarding potential analyzer and cylindrical Langmuir probe, Brown showed the transition from "low-current" to "high-current" modes corresponded to increased electron current to the anode and is therefore related to increased electron transport. Although no physical explanation is offered for the observed transitions, the effect of ambient chamber pressure, cathode flow fraction and augmented xenon flow at the cathode exit hint at a near-field plasma plume mechanism involving neutral density, collision rates and electron mobility for mode transitions without any consideration of wall effects, which is in contrast to the ideas of Gascon and Barral[9].

Further research by McDonald[14] using ultra-fast imaging on the H6 in low-voltage operation was the first to show the transition from "high-current" to "low-current" modes correlated with the formation of spokes. Figure 7 from Ref. 14 shows that strong discharge current oscillations or strong azimuthal oscillations could both be achieved at a discharge voltage of 105 V by variation of cathode flow fraction at constant magnetic field settings. Based on the parametric study, McDonald noted that the operating mode was a stronger function of magnetic field strength than discharge voltage.

In order to understand HETs and develop first-principles based models, the question of anomalous electron transport must be resolved. The transition between modes causes a change in electron current to the anode, implying that understanding mode transitions could offer insight into the unresolved question of anomalous electron transport. Furthermore, tens of kilohertz oscillations where breathing mode oscillations and azimuthal spoke oscillations dominate are likely to play a critical role in electron transport. The previous research cited above suggests two completely different scenarios for mode transition: 1) Plasma interaction with the wall inside the discharge channel; and 2) Near-field plasma plume properties that affect the upstream discharge channel plasma. The research reported on below uses time-resolved plasma diagnostics to study plasma oscillations during induced mode transitions.

III. Experimental Setup

This investigation uses the well-characterized H6 HET to study mode transitions by varying magnetic field strength for various operating conditions. High-speed diagnostics including ultra-fast imaging and probes provide valuable insight into plasma oscillation changes during mode transitions.

A. H6

The H6 Hall thruster shown in Figure 6 is a 6-kW class Hall thruster with a nominal design voltage of 300 V and a 7% cathode flow fraction. It uses a hallow cathode with a lanthanum hexaboride (LaB6) insert that can either be mounted centrally (on thruster centerline which is the nominal configuration) or mounted externally. The inner magnet coil is one, continuously wound solenoid core while the outer coil consists of eight discrete solenoid cores wound in series and separated by 45 degrees. The outer pole is designed such that inside the discharge channel the magnetic field shown in Figure 6 (Right) is azimuthally uniform to less than one Gauss. Note that the magnetic field within the discharge channel cross-section is radially symmetric about (mirrored above and below) discharge channel centerline from the anode to the exit plane, whereas the SPT-100 magnetic field shown in Figure 4 is not. The H6 was a joint development effort of the University of Michigan, the Air Force Research Laboratory (AFRL) at Edwards AFB, and the NASA Jet Propulsion Laboratory (JPL); a separate copy of the thruster is maintained at each institution. It is notable for its high total efficiency; e.g., 64% at 300-V (6-kW) with a specific impulse of 1950 s and 70% at 800-V (6-kW) with a specific impulse of 3170 s.[15] Slightly different nominal operating conditions are used between institutions. At the University of Michigan, work by Reid, Shastry, Huang and McDonald studied operation between 5 and 30-mg/s flow rates, but primarily focused on 20 mg/s for approximately 6-kW operation at 300 V. Work by Hofer at JPL has tuned the H6 to even discharge currents and power levels; i.e., 20 A for exact 6

kW operation at 300 V. For xenon these operating conditions vary only by a few percent in current or mass flow rate (1 mg/s Xe ~ 1 A), but peak magnetic field strengths between the two cases may vary by up to 15%. At the 300-V, 20-mg/s, 6.1-kW Michigan operating condition, the H6 has a 20.3-A discharge current and produces 397 mN of thrust at a specific impulse of about 1900 s.[16] At the nominal 300-V, 20-A, 6-kW JPL condition, the specific impulse is 1950 s with a thrust of 401 mN.[15]

Since first firing in 2006, the H6 has been well characterized by a variety of diagnostic and modeling techniques at Michigan, AFRL and JPL. Six experimental doctoral dissertations have focused on the thruster to date,[16–21] which have spawned numerous associated conference and journal articles. Modeling of the H6 has been performed using the hybrid Particle-In-Cell (PIC) simulation HPHall-2[22] and the more recently developed fluid code Hall-2De.[23] The H6 is a well-characterized HET with multiple references for steady-state values and provides an ideal platform for high-speed investigations of oscillatory plasma phenomena.

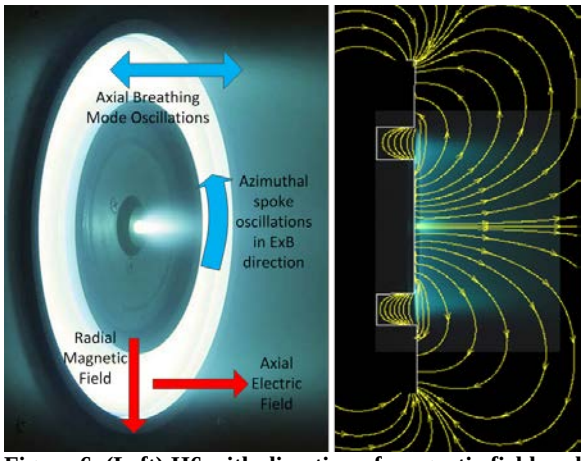

Figure 6. (Left) H6 with direction of magnetic field and E×B shown. (Right) Profile picture of the H6 operating at nominal conditions with magnetic field stream lines overlaid and discharge channel outlined.

Table 1 shows the test matrix for the H6 used in this investigation. Discharge voltages of 300, 400 and 450 V were applied between the anode and cathode. Xenon gas (Research Grade 99.999% pure) was used for the anode and cathode for all testing. Propellant mass flow rates tested were 25.2, 19.5 and 14.7 mg/s through the anode and 1.8, 1.4 and 1.0 mg/s (7% CFF) through the LaB_6 cathode. The flow rate of 19.5 mg/s is the nominal setting used for comparison in this work and the cathode flow fraction of 7% was maintained for all conditions. Centerline cathode mounting is the nominal configuration of the H6 as shown in Figure 6 and Figure 7 (Top), but an external cathode configuration was also tested as shown in Figure 7 (Bottom). The only data presented here for the external configuration are for the nominal 300-V, 19.5-mg/s case. Unless explicitly stated, all data shown below are for the centerline-mounted cathode configuration. The magnetic field shape shown in Figure 6 (Right) was kept constant during testing, though the magnitude, noted by B_r/B_r^*, was varied throughout the testing in order to induce a mode change within the H6. The quantity B_r/B_r^* is the maximum radial magnetic field value at a particular setting of inner magnet (I_{IM}) current and outer magnet (I_{OM}) current (I_{IM}/I_{OM} = 1.12) divided by the nominal maximum radial magnetic field. The nominal magnetic field (B_r^*) strength (i.e., for maximum thruster performance) at 300 V and 20 A discharge current was I_{IM} = 3.50 A and I_{OM} = 3.13 A.[15]

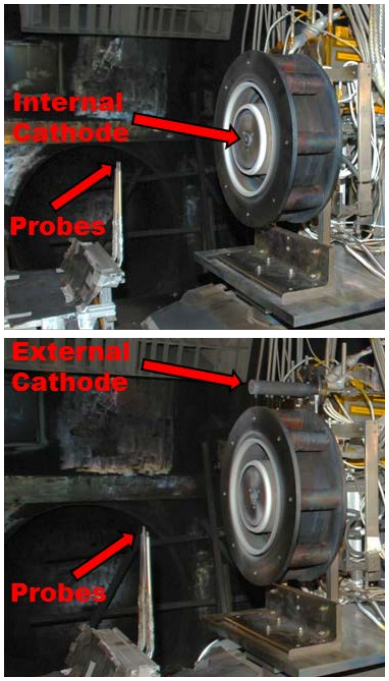

Figure 7. Internal cathode (Top) and external cathode (Bottom) configurations shown with probes.

Table 1. Test matrix showing discharge voltage and anode flow rate variations for the internal cathode configuration. Green: tested, Red: not tested. Number indicates the number of sweeps at the condition.

	14.7 mg/s	19.5 mg/s	25.2 mg/s
300 V	1	4	1
400 V	0	2	0
450 V	0	1	0

In order to confirm the magnetic field magnitude was varied and not direction, magnetic field simulations of the H6 were performed using MagNet Version 7.4.1.4 (32-bit) from Infolytica Corporation for all magnet settings used during B-field sweeps. The peak magnetic field value varied linearly with inner magnet current from the minimum of 1.45 A to approximately the nominal setting of 3.5 A as shown in Figure 8. However, a second order, least squares fit best represents the peak B-field value across the range of magnet coil currents used with the equation shown in Figure 8. The axial location of the peak B-field did not change to within the 2 mm grid used in simulations. Noting that L_{chnl} is the channel length, the maximum deviation of B-field direction within $\pm L_{chnl}/2$ axial distance from the exit plane along the outer wall, channel centerline and inner wall was 6.3, 0.9 and 5.9 degrees, respectively. For $\pm L_{chnl}/4$ axial distance from the exit plane the maximum deviations were 1.8, 0.3 and 1.9 degrees, respectively. Based on the internal measurements of Reid,[16] most of the ionization and acceleration occurs within the axial region approximately $\pm L_{chnl}/4$ from the exit plane. Therefore, the magnetic field shape shown in Figure 6 can be considered constant throughout sweeps and the resulting mode transitions are due solely to the magnitude change. This conclusion will be further supported by the fact that mode transitions across different operating conditions do not occur at any one preferential magnetic field setting.

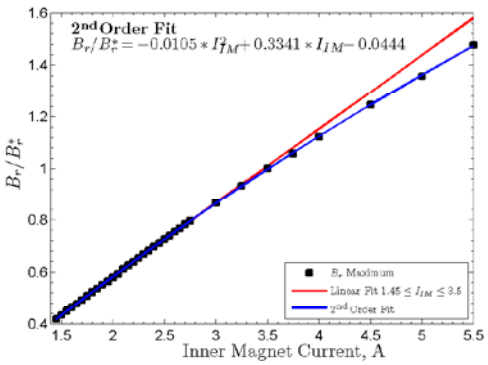

Figure 8. Normalized maximum radial magnetic field (B_r/B_r^*) on channel centerline as a function of inner magnet current (I_{IM}). A linear least squares fit from the minimum current to the nominal setting is shown as well as a 2nd order least squares fit over the entire range.

B. Facilities and Thruster Performance Monitoring

This investigation was conducted in the Large Vacuum Test Facility (LVTF) of the Plasmadynamics and Electric Propulsion Laboratory (PEPL) at the University of Michigan. The LVTF is a 200 m^3 stainless steel-clad vacuum chamber 9 m long and 6 m in diameter. Rough vacuum is achieved with two 2000 CFM blowers backed by four 400 CFM mechanical pumps with a final base pressure in the low 10^{-7} Torr achieved by seven CVI TM-1200 re-entrant cryopumps with LN_2 baffles and a nominal pumping speed of 500,000 L/s on air or 245,000 L/s on xenon. During thruster operation, the chamber pressure is measured with a nude ion gage at the top of the chamber downstream of the thruster location with an uncertainty of $\pm 0.1\times10^{-6}$ Torr. Pressure varied for conditions based on anode flow rate but with a fixed chamber pumping speed. The xenon corrected pressures were 6.1×10^{-6}, 9.0×10^{-6} and 1.2×10^{-5} Torr for 14.7, 19.5 and 25.2 mg/s anode flow rate, respectively. Discharge voltage and current to the thruster were supplied with an Amrel 100-kW DC power supply across a 102-mF Maxwell Laboratories Caster Oil capacitor. Telemetry including mean discharge current, cathode-to-ground voltage, discharge voltage, inner and outer magnetic coil currents and voltages was measured at 1-s intervals with an Agilent 34970A Data Logger and recorded on a computer using Agilent Benchlink software. The discharge voltage (V_D) was measured using sense lines on the anode and cathode. Sense line raw voltage signals were sent to a 10,000:1 voltage divider that was calibrated with a BK Precision 5491A multimeter. Mean discharge current $\overline{I}_D = \langle I_D(t) \rangle$ where $\langle\ \rangle$ denotes the average was measured with an NT-50 FW Bell sensor. Magnet coil currents were measured with 10-mΩ shunt resistors. All currents were calibrated using a precision 10-mΩ resistor accurate to 0.1% and a BK Precision 5491A multimeter. Plume photographs were taken with a Nikon D80 digital camera with a DX AF-S Nikkor 18-135 mm lens set to f5.6, 1/100 s shutter speed and manual focus.

The xenon propellant is delivered to the HET using Alicat Scientific MC Series mass flow controllers through electro-polished stainless steel lines. Mass flow calibration takes place through a Bios Definer 220L DryCal system plumbed in parallel to the anode and cathode feed lines with a measurement accuracy of 1% of the reading between 5 and 500 sccm. Mass flow calibrations are taken for each mass flow controller at several flow rates and a linear fit is used to determine the flow produced at any arbitrary set point. The AC component of the thruster discharge current, $I_{D\,AC}(t)$ was measured either with a Tektronix TCP 312 (DC to 100-MHz bandwidth) or TCP 303 (DC to 15-

MHz bandwidth) split-core Hall current sensors through a Tektronix TCPA 300 current probe amplifier. The signal was measured on the discharge current line external to the chamber on the anode side and was acquired simultaneously with Langmuir probe (HDLP-ISR) signals on the same Data Acquisition (DAQ) system described later. The total discharge current, time history signal is the combination of the two measurements

$$I_D(t) = \bar{I}_D + I_{D_{AC}}(t). \tag{2}$$

Discharge current oscillation amplitude will be defined here as the root-mean-square (RMS) of the AC component of the discharge current time history signal in amperes

$$\tilde{I}_D = \sqrt{\left\langle \left(I_D(t) - \bar{I}_D \right)^2 \right\rangle} = \sqrt{\left\langle I_{D_{AC}}(t) \right\rangle^2} \tag{3}$$

Note that Eq. (3) is the square root of the sample variance for a sample size N and not the square root of the bias-corrected variance which would have $\sqrt{N-1}$ in the denominator. The difference is negligible for the discharge current signal where the sample size N is between 1×10^6 and 45×10^6 points. The relative discharge current oscillation amplitude is the RMS value fraction of the mean discharge current $\tilde{I}_D / \bar{I}_D$. The normalized, AC component of the discharge current, $\hat{I}_D(t)$, is calculated from the discharge current time-history signal, by

$$\hat{I}_D(t) = \frac{I_D(t) - \bar{I}_D}{\tilde{I}_D}. \tag{4}$$

Discharge current density average $\bar{j}_D$ and time history $j_D(t)$ values are defined as

$$\bar{j}_D = \frac{\bar{I}_D}{A_{chnl}} \tag{5}$$

$$j_D(t) = \frac{I_D(t)}{A_{chnl}} = \frac{\bar{I}_D + I_{D_{AC}}(t)}{A_{chnl}} \tag{6}$$

where $A_{chnl} = \pi\left(r_o^2 - r_i^2\right)$ is the area of the discharge channel with outer and inner radius, r_o and r_i, respectively.

PEPL uses an inverted pendulum thrust stand based on the NASA Glenn Research Center design of Haag[24] to measure thruster performance. This design has extensive heritage for testing electric propulsion devices[16,19,25] so the details will not be recapitulated here. In summary, the inverted pendulum thrust stand operates in null mode using a Proportional, Integral, Derivative (PID) controller and a solenoid actuator to maintain the pendulum in a vertical position based on feedback from a Linear Variable Differential Transformer (LVDT). The thrust stand tilt must remain constant throughout operation, which can shift during pump down and thruster operation due to thermal expansion of structural components. An inclinometer is used to monitor thrust stand tilt and manual adjustments are made with a control motor as necessary. A cooling loop with glycol powered by a Polyscience Durachill 6860T chiller with 5.2-kW cooling capacity is used to thermally regulate the thrust stand. The thruster was operated for over three hours before any data were acquired in order for the thruster and thrust stand to reach thermal equilibrium. Even if the thrust stand were not at complete thermal equilibrium, this is accounted for by taking zero values at regular intervals where the thruster is briefly turned off and the zero output is recorded. The thrust stand was calibrated by lowering and raising a series of high-precision weights to ensure a linear response. Calibration was performed before thruster operation, two times during testing when the thruster was briefly turned off, and once again after testing was complete. All calibrations showed a linear response and were combined to generate the thruster calibration curve to convert PID controller output in volts to thrust in mN.

C. Probes

A pioneering technique for time-resolved plasma property measurements at 100's kHz[26] has been developed by Lobbia called the High-Speed Dual Langmuir Probe (HDLP).[27] The technique was recently augmented with an Ion Saturation Reference (ISR) probe[28] to calculate ion density and provide the HDLP signal with a DC reference. Each HDLP-ISR consists of an active probe, a "null" probe that corrects for capacitance effects from rapid sweeping and

the ISR probe as shown in Figure 9. Both the active and null probes were 0.13-mm-diameter pure tungsten wire with 3 mm exposed for the active HDLP probes and ISR probes; the null probe by design does not have any exposed wire.

The ISR signal alone can provide useful information for identifying plasma oscillations without actually calculating plasma properties and is the only data reported here. The time-resolved plasma property measurements of electron density, plasma potential and electron temperature will be reported in a future publication. According to thin sheath Langmuir probe analysis,[29,30] I_{ISR} is linearly related to ion density at constant electron temperature if the probe is operated in ion saturation

$$n_i = \frac{I_{ISR}}{0.605 A_p e \sqrt{eT_e / m_i}} \tag{7}$$

where n_i is the ion density, A_p is the probe area, I_{ISR} is the probe current at ion saturation, T_e is the electron temperature in eV and e is the elementary charge. Previous work mapped the plasma plume of the H6 with a discharge voltage of 300 V and discharge current of 20 A for the nominal magnetic field, $B_r/B_r^* = 1$.[28] Using the plume information from Figures 14 and 15 of Ref. 28, the electron temperature and plasma potential are 3.7 eV and 30 V with respect to ground. In order to ensure the ISR probes are in ion saturation, they must be biased well below the floating potential, which from Eq. (7) of Ref. 28 is

$$V_f \approx V_p - 5.8 T_e \tag{8}$$

The ISR probes were biased to -30 V with respect to ground, which is more than 16 T_e below the plasma potential and therefore are safely in ion saturation. During this investigation, the magnetic field, discharge voltage and flow rate were varied, so the plume properties will differ from those reported in Ref. 28. However, with a factor of 3 margin (16 T_e vs. 5.8 T_e) at nominal conditions, the probes are still expected to be in ion saturation at the off-nominal conditions.

The ISR current is measured external to the LVTF across a 100-Ω shunt resistor through an Analog Devices AD 215 120-kHz low-distortion isolation amplifier.[†] The data acquisition system used to record discharge current and the ISR signals are sampled at rates up to 180 MHz with 16-bit AlazarTech ATS9462 digitizers. The probes were positioned using a 1.5-m-long Aerotech ATS62150 ball screw stage driven by a stepper motor and controlled with an Aerotech MP10 controller. The probe table was used in open loop position feedback mode with a 15-V string potentiometer to monitor the stage position during movement and ensure proper positioning in front of the thruster to within 5 mm radially. Figure 9 shows the two HDLP-ISRs in position in front of the thruster 1.5 mean channel radii downstream in the 6 o'clock position on discharge channel centerline (within ±5 mm). The ISR probe gap was 29.5 ±0.5 mm apart, which corresponds to 21.4° ±1.7° of azimuthal spacing; i.e., ~11° on either side of 6 o'clock.

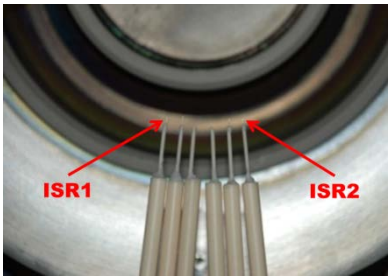

Figure 9. Two HDLP-ISR probes in position at the 6 o'clock location. A complete HDLP-ISR consists of an active probe, a null probe and an ISR probe. The exposed Tungsten wire is only near the arrow tip.

The Pearson linear correlation coefficient or product-moment coefficient of correlation ρ_{xy} is used to quantify how well two signals, x and y, are linearly correlated[31]

$$\rho_{xy} = \frac{\sum_N \left(x_i - \langle x \rangle\right)\left(y_i - \langle y \rangle\right)}{\sqrt{\sum_N \left(x_i - \langle x \rangle\right)^2 \sum_N \left(y_i - \langle y \rangle\right)^2}} \tag{9}$$

This technique will be used to show the correlation of the discharge current with the ISR probe signals and of probe signals. The coefficient ranges from $-1 \le \rho_{xy} \le 1$ where 1 means the signals are perfectly correlated ($x = y$), -1

[†] The 2-μs offset called out on the data sheet was verified using a Tektronix AFG3010 function generator and a Tektronix digital oscilloscope, and accounted for in our experiments.

means they are inversely correlated ($x = -y$) and 0 means they are not correlated. Additionally, the cross-correlation is used extensively to calculate the time-offset between two signals. The cross-correlation function is[31]

$$R_{xy} = \lim_{T\to\infty} \frac{1}{T} \int_0^T x(t)\, y(t+\tau) dt. \tag{10}$$

Signal delays for non-frequency dispersive propagation can be identified by peaks in R_{xy} as is done with discharge current and probe signals. When calculating R_{xy} from Eq. (10), the AC component is isolated by subtracting the mean and then normalized by dividing by the RMS value; the time delay is determined from the largest peak in R_{xy}.

IV. High-speed Imaging Analysis

A high-speed image analysis technique was developed by McDonald[20,32,33] to investigate azimuthal oscillations from videos. Here the McDonald technique has been adapted to transform the videos into measurements of discharge current density distribution in the discharge channel in order to quantify oscillations. These techniques will be referred to as High-speed Image Analysis (HIA) throughout the following discussion.

A. Equipment and Image Enhancement

High-speed imaging was acquired with a Photron SA5 FASTCAM with a Nikon ED AF Nikkor 80-200 mm lens at its maximum aperture f/2.8. The SA5 is capable of up to 1,000,000 fps with 128×16 pixel resolution, but was used at 87,500 fps with 256×256 pixel resolution for this testing. The camera was 6 m downstream from the thruster outside LVTF with a view of the thruster through a viewport. The image enhancement technique developed by McDonald[33] allows for easy visualization of rotating spokes as shown in Figure 10. When watching the raw FastCam video the rotating spokes are very clear to the casual observer; the visualization technique shown in Figure 10 is only meant to enhance what is unambiguously present. Here small fluctuations in light intensity from a mean value can be seen and have been shown to rotate in the E×B direction as azimuthally propagating spokes. It is important to note that the pixel value corresponding to light intensity is not a direct measure of plasma properties. However, if light is assumed to be produced primarily by collisional processes then the brightness should be related to collision rates and densities as will be discussed later. Also important is that the camera records an integrated light intensity through the plume to the anode, meaning it cannot distinguish where the brightest regions of the plume are located axially.

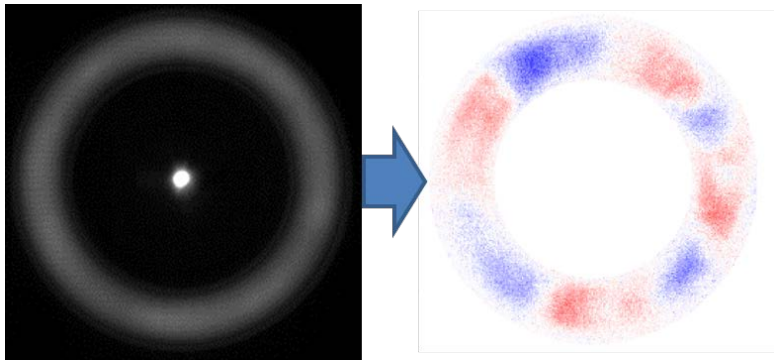

Figure 10. Raw FastCam video frame and subsequent enhancement with the McDonald technique to visualize spokes.

B. Analysis Method

The Fourier analysis techniques developed by McDonald[32] have been adapted to process the FastCam videos to determine breathing and spoke mode frequencies. The high-speed imaging technique consists of the following eight (8) steps:

1. Import the raw video file into MatLab as a $p(x, y, t) = 256 \times 256 \times N_f$ matrix, where N_f is the number of frames in the video. The Photorn SA5 has a 12-bit sensor, so each pixel, p, has 2^{12} =4096 possible values assumed to linearly represent light intensity. McDonald notes that raw pixel output is non-linear at high incident fluxes to the camera, but by design the "high frame rates used [imaging HETs] are sufficient to keep the light intensity reaching the camera well inside the linear regime."[32] The cathode region saturates and becomes non-linear, but that is not used in this analysis so it is negligible. The light from the discharge channel critical for this analysis remains within the linear region of pixel output and the assumption is justified.

2. Calculate and subtract the mean image $\bar{p}(x,y)$ from each frame in order to isolate the AC component of the video $\tilde{p}(x,y,t) = p(x,y,t) - \bar{p}(x,y)$. The mean image is a 256×256 matrix where each pixel has been averaged across all N_f frames. Subtracting the mean image to isolate the AC component removes any DC bias for pixel values and is discussed in more detail at the end of this section with an example shown in Figure 11.
3. Automatically identify the center of the circular discharge channel using a Taubin circle fit and isolate the annular region of the discharge channel in each frame.
4. Considering the pixels in cylindrical coordinates $\tilde{p}(x,y,t) \rightarrow \tilde{p}(r,\theta,t)$, divide the annulus into N_b= 180 two-degree bins, *b*, and determine which pixels from the 256×256 array belong to each bin. Each bin has M_b = 120 to 160 pixels.
5. Average the pixel value for each bin to generate a 180×1 vector of light intensity values for each frame.

$$a(b,t) = \frac{\sum_{r=r_i}^{r_o} \sum_{\theta=\theta_b}^{\theta_{b+1}} \tilde{p}(r,\theta,t)}{M_b} \tag{11}$$

6. Calculate the $m = 0$ or m_0 spoke order, which is the entire channel added together.

$$m_0(t) = \sum_{b=1}^{N_b} a(b,t) \tag{12}$$

7. The discharge current is linearly related to the $m_0(t)$ spoke order as first shown by Lobbia[34] and will also be shown later (in Figure 16). The discharge current $I_D(t)$, which has a native bandwidth above 1 MHz, is down-sampled to the camera frame rate of 87.5 kHz using an 8th order Chebyshev Type 1 filter to smooth and resample. Apply a linear, least squared fit to relate I_D to m_0, where c_1 and c_2 are the resulting linear coefficients. Note, the total discharge current $I_D(t)$ can be written as the sum of the discharge current through each bin, $I_{D_b}(b,t)$. Assuming the offset coefficient, c_2, can be equally distributed amongst the bins allows it to be included in the summation. The discharge current can then be written as

$$I_D(t) = \sum_{b=1}^{N_b} I_{D_b}(b,t) = c_1 m_0(t) + c_2 = \sum_{b=1}^{N_b} \left(c_1 a(b,t) + \frac{c_2}{N_b} \right) \tag{13}$$

Assuming that local light intensity is linearly related to local discharge current, each element of the summation in Eq. (13) can be equated. The local discharge current density j_{D_b} for bin *b* is then

$$j_{D_b}(b,t) = \frac{I_{D_b}(b,t)}{A_b} = \frac{c_1}{A_b} a(b,t) + \frac{c_2}{A_b N_b} \tag{14}$$

While the linear relation in Eq. (13) between the global variables I_D and m_0 are well supported in the results, the assumption of a linear relation between local light intensity and local discharge current at present only has indirect support. This assumption will be discussed at length in Sections IV E and VI B. The discharge current density surface is a 180×N_f matrix for the angular discharge current density over time as shown in Figure 11 (c) and discussed in more detail below with uncertainty analysis.
8. Perform a 2-D discrete Fourier transform (DFT) on the discharge current density surface to compute frequency and order number. The magnitude of the 2-D DFT generates a PSD surface map of frequency (1/s) versus 1/deg or 1/rad using Eq. (21) as discussed below. The angular location is converted to spoke order (*m*), which are the number of spokes present in the channel and are shown in Figure 17 and Figure 18.

The light observed by the FastCam is integrated through the plume and through the discharge channel to the anode at the back of the discharge channel. Photographs from angles nearly orthogonal to thruster centerline (e.g. Figure 22 and Figure 23 in Section V E) show the plasma in the discharge channel is significantly brighter than the plume. Even though the path length through the plume is longer than the path length through the discharge channel,

the brighter discharge channel generates most of the light recorded by the FastCam. The camera is vertically level with the thruster and offset horizontally with an angle of 2.5 degrees to the left of thruster centerline and has a more direct view of the 6 to 12 o'clock side of the channel. Even though the view of the discharge channel 3 o'clock region will be integrated through more of the plume, part of the discharge channel will be masked and could appear dimmer to the camera. The inner channel wall and near-anode region within ~2 mm of the thruster inner diameter will be blocked from the camera at 3 o'clock, which is less than 3% of the discharge channel radial-axial cross-section. However, light producing collisions and plasma oscillations are not expected to be significant in these masked areas compared to the discharge channel exit plane where the bulk of ionization and other collisional processes occur. Isolating the AC component of pixel value as in Step 2 will remove any constant pixel brightness differences that may occur due to these offset or other factors.

Figure 11 (a) shows an example plot of average pixel value per bin, $a(b,t)$ from Eq. (11), that would be produced in Step 5 without executing Step 2 to isolate the AC component. Figure 11 (b) shows the average pixel value per bin when all steps are executed and very little difference is observed with Figure 11 (a) other than scale change. Figure 11 (c) shows an example current density plot that is produced in Step 7, which also retains all of the same features as Figure 11 (a) and (b) with only a scale change. It is important to note that the calculation of discharge current density does not alter the features of the Spoke Surface plots that McDonald originally developed during his analysis so those techniques for calculating PSDs remain valid and comparable.

C. Uncertainty Analysis

Significant error or uncertainty can be introduced with the assumptions above, and an attempt to quantify the uncertainty is presented here. Three primary sources of uncertainty will be considered, other sources of uncertainty such as probe resolution, calibration uncertainty, model uncertainty and linearity of camera response are assumed to be of lower order.

1. Standard deviation of pixel values in bin b from the mean pixel value, a. This will be different for each bin b and time t.
2. Error from the linear fit of $m_0(t)$ to $I_D(t)$, which will vary in time but be applied equally for each bin b.
3. Difference between $I_D(t)$ at the native sampling rate or full bandwidth of the current probe (whichever is lower) and $I_D(t)$ down-sampled to the camera frame rate. This will vary in time but also be applied equally for each bin b.

The total error in j_{D_b} is the sum of the three error sources considered above:

$$\sigma_{j_{D_b}}(b,t) = \sigma_{j_{D_b}1}(b,t) + \sigma_{j_{D_b}2}(t) + \sigma_{j_{D_b}3}(t). \tag{15}$$

The standard deviation for the pixel value in bin b is computed similar to how the average value is calculated in Eq. (11).

$$\sigma_a(b,t) = \left[\frac{1}{M_b - 1} \sum_{r=r_i}^{r_o} \sum_{\theta=\theta_b}^{\theta_{b+1}} \left(\tilde{p}(r,\theta,t) - a(b,t) \right)^2 \right]^{1/2}. \tag{16}$$

Using the error propagation equation[35] on Eq. (14) yields

$$\sigma_{j_{D_b}1}(b,t) = \frac{\partial j_{D_b}}{\partial a} \sigma_a(b,t) = \frac{c_1}{A_b} \sigma_a(b,t) \tag{17}$$

where the error in c_1 and c_2 will be accounted for in $\sigma_{j_{D_b}2}$.

The error in linear fit between I_D and m_0 is estimated using built in MatLab functions (`polyfit` and `polyval`) while calculating the least-squared coefficients c_1 and c_2. The estimate of the standard deviation of the error at each point is calculated using the triangular factor of the Vandermonde matrix, the degrees of freedom and the norm of the residuals.[36] Assuming the error in measurements is independent with constant variance, the uncertainty

estimates $\Delta I_D(t)$ will encompass 50% of predictions in I_D from m_0. The uncertainty $\sigma_{j_{D_b}2}$ introduced by the linear fit between I_D and m_0 is

$$\sigma_{j_{D_b}2}(t) = \frac{\Delta I_D(t)}{A_{chnl}}. \tag{18}$$

The discharge current I_D is filtered and down-sampled to correlate with m_0 as described in Step 7. It is then up-sampled using interpolation to calculate the difference with the native I_D. The difference is resampled at the camera frame rate without smoothing or filtering in order to determine the difference between native and down-sampled discharge current.

$$\sigma_{j_{D_b}3}(t) = \frac{\left|\{I_D(t)\}_{Native} - \{I_D(t)\}_{DownSampled}\right|}{A_{chnl}}. \tag{19}$$

For a mean discharge current of $\overline{I}_D = 20\text{A}$ the average discharge current density is $\overline{j}_D = 133\text{mA/cm}^2$. An error of 1 A in discharge current for Eqs. (18) or (19) yields an uncertainty of 6.6 mA/cm^2 for $\sigma_{j_{D_b}2}$ or $\sigma_{j_{D_b}3}$. Regardless of the uncertainty introduced, the method outlined above provides meaningful quantification of FastCam images to discuss oscillation amplitudes during mode transitions.

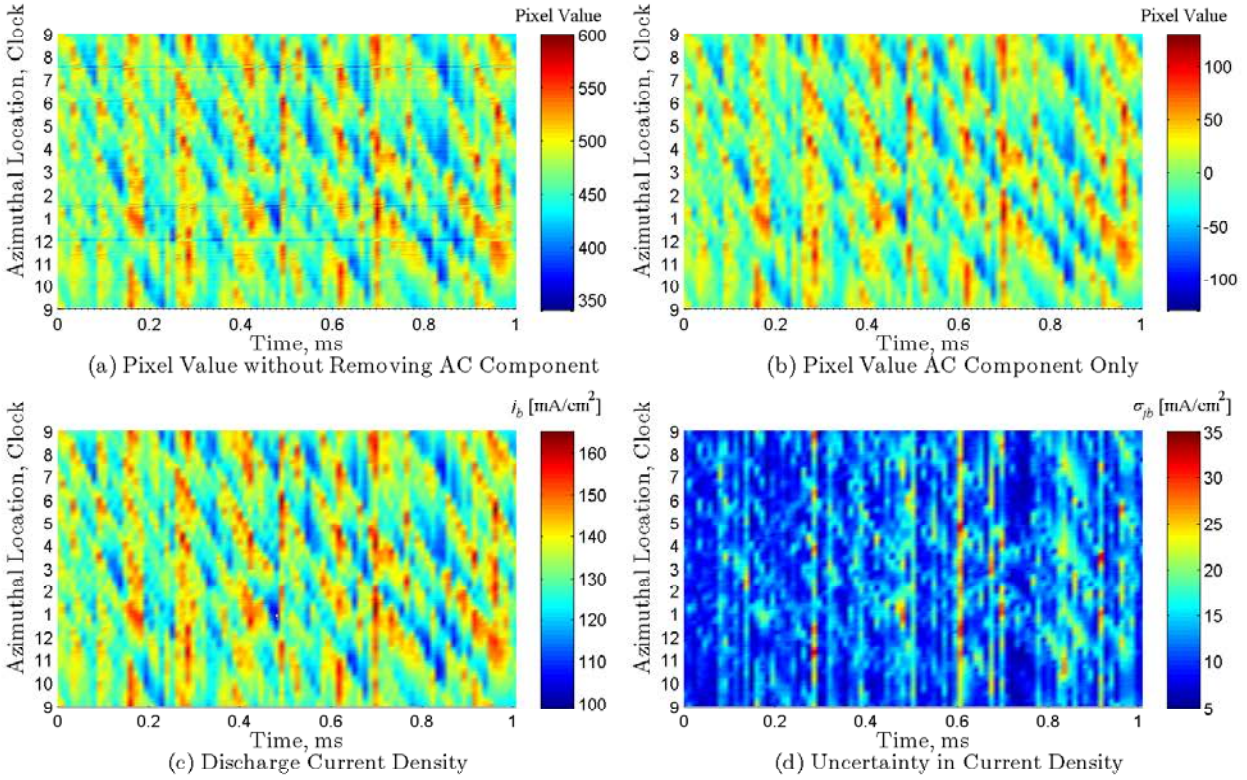

Figure 11. Surface plots for 300 V, 19.5 mg/s, B_r/B_r^* = 1. (a) Average pixel values from Eq. (11) without executing Step 2 to isolate the AC component; note the horizontal lines present for some bins, (b) AC component of average pixel values calculated in Step 5; the pixel values oscillate about zeros but all features and amplitudes are retained from (a), (c) Discharge current density plot calculated in Step 7 from Eq. (14) which retains all features of (c), (d) Uncertainty in discharge current density calculated from Eq. (15).

An example of a discharge current density surface plot calculated from Eq. (14) is shown in Figure 11(c) with the uncertainty calculated from Eq. (15) shown in Figure 11(d). In the discharge current density surface plot, the

ordinate is azimuthal location around the discharge channel in clock positions and the abscissa is time with each vertical column of values representing one frame of video. Vertical features in the discharge current density surface plot represent extremes in discharge current density that occur everywhere in the channel simultaneously. Horizontal features would be discharge current values that remain constant at a fixed azimuthal location, which is not typically observed because they are removed in Step 2. Diagonal features are perturbations in discharge current density that propagate azimuthally around the discharge channel. Lines from upper-left to lower-right are propagating counter-clockwise around the discharge channel and lines from the lower-left to upper-right are propagating clockwise. The E×B direction in the H6 is counter-clockwise since the B-field direction is radially out. It will be shown later that all azimuthally propagating features are in that direction represented by lines from upper-left to lower-right with the slope corresponding to propagation velocity in deg/s. While in global mode, the discharge current rises in approximately 20-40 μs as shown in Figure 19, but the FastCam frame rate of 87,500 fps yields a resolution of 11.4 μs which introduces error while matching m_0 and I_D in Eq. (18). The surface plots of discharge current density (e.g. Figure 11(c)) have the same features and look identical to the spoke surface plots developed by McDonald[32] due to the linear scaling. However, the scaling adds physical units and is useful to investigate and visualize global discharge channel oscillations as well as azimuthally rotating spokes.

D. Power Spectral Density

Several methods can be used to describe the frequency response of a signal, so here we define the methods and formulas used below. If *X(f)* is the 1-D discrete Fourier transform (DFT) of a time-series signal *x(t)* with length *N*, then the periodogram spectral estimate $S_N(f)$ of the signal,[37] which is an estimate of the power spectral density (PSD) without scaling,[38] is

$$PSD_{1D}(f) = S_{N1D}(f) = \frac{1}{N} X^*(f) \cdot X(f) \tag{20}$$

where $X^*(f)$ is the complex conjugate. A 2-D DFT of the discharge current density surface plot $j_{D_b}(t,\theta)$ produces $J_{D_b}(f,\gamma)$ where γ is in units of 1/deg. Fourier transforms can be extended to multiple dimensions, so by analogy to Eq. (20) the 2-D PSD is

$$PSD_{2D}(f,\gamma) = S_{N2D} = \frac{1}{N_f N_b} J^*_{D_b}(f,\gamma) \cdot J_{D_b}(f,\gamma). \tag{21}$$

The analysis of PSDs below only compares the change in relative magnitude of the PSDs through mode transitions, so without proper scaling on Eqs. (20) and (21) the units will be listed as Arbitrary Units/Hz in Figure 17 and Figure 18. In a 2-D Fourier transform of a surface where one axis is time and the other is angle (degrees), one axis of the transformed surface will be similar to a typical 1-D Fourier transform of a time history signal with units of f = 1/s or Hz and the other will yield γ = 1/deg. Multiplying γ by 360 deg/circle yields the spoke order m or number of segments per circle (e.g. m = 3 means three segments or three spokes). As described by McDonald in his original derivation,[32] this is analogous to number of wave lengths per channel circumference. Hence m = 0 or m_0 is no wave in the channel (the entire channel is dark or bright), m = 1 means one wave in the channel (one half bright, the other dark), m = 2 is two waves per channel (two bright regions, two dark regions), m = 3 is three waves per channel (three bright regions, three dark regions), etc. Eq. (20) is used to calculate the PSDs for the AC components of discharge current and ISR probe current, which removes large value at f = 0 when there is a DC offset. When computing the 1-D DFT for $I_{D_{AC}}$ and I_{ISR} a Blackman window is used and when computing the 2-D DFT of j_{D_b} a Hamming window is used.

E. Support for Local Light Intensity Correlation to Local Discharge Current

The most direct evidence for the assumption that local light intensity is linearly related to local discharge current density in order to justify Eq.(14) from (13) would be a direct, linear correlation between FastCam images and current from a segmented anode, which is not presently available. However, McDonald[32] conducted an

investigation using a 12-segment anode in the H6 and used the same Photron SA5 FastCam where he concluded that "visible rotating spokes detected via high speed camera correspond to azimuthally localized electron current deposition to the anode." Comparison of Figure 12 to Figure 13 in Ref. 32 shows the peaks in the PSD of an individual anode segment match the peaks in the PSD from high-speed image analysis, neither of which match the global discharge current or $m = 0$ PSD. This indicates the anode segments are observing local current oscillations that are not present in the global discharge, but are observed as azimuthal oscillations with the FastCam. Figure 9 from Ref. 32 shows the time history of segment current signals where the time delay between signals of adjacent segments is interpreted to be the result of passing spokes. The time delay between signals can be estimated as approximately ~0.05 ms to travel 3 segments which corresponds to 1/6 - 1/4 of the discharge channel circumference. This yields a very reasonable spoke velocity between 1700 and 2500 m/s. Figure 12 from Ref. 32 shows a PSD from high speed image analysis with three primary spoke orders: $m = 4$ at 14 kHz, $m = 5$ at 18 kHz and $m = 6$ at 23 kHz. The relation between spoke order and azimuthal wave number, k_θ, in rad/m is $m = k_\theta r$ where r is the mean discharge channel radius. The phase velocity is $v_{ph} = \omega/k$ where ω is the frequency in rad/s. A plot of ω versus k_θ (not shown) yields a linear relation with a slope of 2100 m/s that matches well with the spoke velocity calculated from the estimated time delay of anode segment signals. While not direct evidence that local light intensity is linearly related to local discharge current, this does provide evidence that the local discharge current oscillations are related to azimuthal light fluctuations in the discharge channel.

Additional, indirect, support for the assumption that local light intensity is linearly related to local discharge current density is provided by the correlation of light intensity fluctuations to downstream electron density oscillations. In a study using a BHT-600 thruster, Lobbia[34] correlated high-speed imaging results with downstream high-speed Langmuir probe measurements of electron density, plasma potential and electron temperature. This analysis shows total light intensity for the portion of the discharge channel imaged with a Photron FastCam-1024-PCI (only ~50% of the discharge channel is imaged) at 109,500 fps is correlated to discharge current and electron density oscillations downstream using linear, frequency domain transfer functions. In processing the FastCam images, Lobbia used an integrated, normalized image intensity which effectively gives the $m = 0$ order described here. The correlation was observed at the strong 18.4 kHz breathing mode and no attempt was made to analyze azimuthal variations although they were qualitatively noted. The location of the probes was varied from 3 to 11 thruster diameters downstream with a linear relation shown throughout. The assumption can be made that the increased electron density (and corresponding ion density invoking the assumption of quasi-neutrality) is produced in the discharge channel which then propagates axially downstream, so the light intensity correlates to electron density oscillations in the channel. This assumption makes physical sense as Lobbia[34] noted that in the discharge channel the "unsteady emission of photons generated by increased atomic state transitions [are] associated with the bursts of ionization." Further evidence for the correlation between light intensity and ion density using the ISR probes from this investigation will be discussed later in Section VI B, which reinforces the initial findings of Lobbia.

Now consider the relation between optical emission (light) intensity and the physical processes occurring in the discharge channel. Plasma spectroscopy can be used to calculate neutral densities and electron densities[39] using a given plasma model (e.g. thermal equilibrium, coronal equilibrium, collisional-radiative, etc). Assume the plasma is in coronal equilibrium where all upward transitions in atomic energy state (excitations) are collisional and all downward transitions are radiative. Also assume the plasma is optically thin so all emitted photons escape the plasma and are not reabosrbed.[40] Finally, assume the time constant, τ, for this equilibrium is faster than the 10's kHz oscillations considered here so $\tau << 100\ \mu s$. In equilibrium, the emission of radiation from atoms or ions in an excited state will balance the collision frequency that produced the excited state. [40] This means light emission will be related to electron density, neutral density and ion density. Ref. 41 shows that optical emission intensity due to excitation from ground state is linearly related to the free radical density and in Ref. 39 continuum emission coefficients are linearly related to electron and ion densities. We assume that fluctuations in optical emissions are linearly related to oscillations in electron and neutral densities to first order. This assumption implies that the electron energy distribution is Maxwellian and remains constant during plasma oscillations.. Plasma spectroscopy

has a rich theoretical and experimental history[39,40] and a more rigorous derivation of the optical emission intensity relation to electron, ion and neutral density in the discharge channel will be addressed in a future work.

Having made the reasonable assumption that light intensity fluctuations are linearly correlated to density oscillations in the channel, an argument can be made that oscillations in local discharge current density, j, are linearly related to electron density n_e and neutral density N fluctuations to first order with a common relation

$$j = en_e \mathrm{v}_{z-eff} \tag{22}$$

where $\mathrm{v}_{z\text{-}eff}$ is an effective cross-magnetic field, axially directed, electron velocity. This makes the reasonable assumption that discharge current is entirely composed of electron current to the anode.[42] However, $\mathrm{v}_{z\text{-}eff}$ is a complicated and unknown function of density, magnetic field and other parameters. Indeed, researchers have been attempting to understand cross-field electron transport since the inception of HETs and have various explanations including, but not exclusive to: classical cross-field diffusion, Bohm diffusion, turbulence, shearing,[43] near-wall conductivity[1] and azimuthal electric fields.[44,45] Linearizing Eq. (22) with mean (bar) and oscillatory values (tilde) and neglecting second order terms the local discharge current density can be written as

$$j = \bar{j} + \tilde{j} = e\bar{n}_e \bar{\mathrm{v}}_{z-eff} + e\bar{n}_e \tilde{\mathrm{v}}_{z-eff} + e\tilde{n}_e \bar{\mathrm{v}}_{z-eff} \tag{23}$$

In order to justify the assumption that $\tilde{j} \sim \tilde{n}_e, N$ to first order, Eq. (23) shows that $\tilde{\mathrm{v}}_{z-eff}$ must also be linearly related to $\tilde{n}_e$ and N to first order. The derivation only considering classical cross-field diffusion is provided in the Appendix with corresponding assumptions where Eq. (39) shows $\tilde{\mathrm{v}}_{z-eff} \sim \tilde{n}_e, N$ to first order neglecting oscillations in electric field and electron temperature. For azimuthal electric fields, E_θ, the derivation of Yoshikawa[44] as discussed by McDonald[32] derived an analytical expression for the local current density due $E_\theta \times B_\mathrm{r}$ drifts

$$j(\theta) = \frac{e\pi}{4B} E_z \left(\tilde{n}_e \sin(\theta) + \frac{\tilde{n}_e^2}{\bar{n}_e} \sin^2(\theta) \right) \tag{24}$$

where the linearized density is $n_e = \bar{n}_e + \tilde{n}_e \sin(\theta)$. Eq. (24) also shows that *local* discharge current density is linearly related to $\tilde{n}_e$ to first order after neglecting the second order $\tilde{n}_e^2$ term. When integrating Eq. (24) around the discharge channel from $0 \to 2\pi$ to calculate the average current density over the entire channel due to azimuthal electric fields, the $\sin(\theta)$ integrates out and the result is

$$\bar{j} = \frac{e\pi}{8} \frac{E_z}{B} \frac{\tilde{n}^2}{\bar{n}_e} \tag{25}$$

Therefore the *average* discharge current density is related to the square of the oscillation amplitude for cross-field current due to azimuthal electric fields.

It is very important to note the derivation shown in the Appendix and the above relation from Yoshikawa are *not* meant to be all-inclusive models of electron transport in the discharge channel of a HET, which even far more sophisticated models cannot reproduce accurately. Also when considering near-wall conductivity, turbulence and shearing, the relation may not be linear between $\tilde{\mathrm{v}}_{z-eff}$, $\tilde{n}_e$ and N. The sole purpose of this derivation and discussion is to reasonably justify the assumption that to first order the local discharge current density oscillations are linearly related to local density oscillations which are linearly related to light intensity oscillations in order to support the assumption used to derive Eq. (14) from (13).

V. Results

The measurement tools and data analysis techniques described above were used to analyze mode transitions intentionally induced in the H6 by varying magnetic field magnitude. Magnetic field sweeps, or B-field sweeps denoted by B_r/B_r^*, were conducted with all other parameters including discharge voltage, flow rate and chamber pressure, held constant until the thruster transitioned modes and eventually became unstable. For reasons that will be made clear and discussed in great detail below, the B_r/B_r^* region of decreased discharge current mean and oscillation amplitude will be called local oscillation mode and the B_r/B_r^* region of increased discharge current mean and oscillation amplitude will be called global oscillation mode.

A. Transition

The magnetic field was varied by changing the inner and outer magnet coil currents in a constant ratio with all other parameters held constant including flow rates, discharge voltage, and chamber pressure. Maintaining a constant 1.12 ratio of inner to outer coil current allowed the magnetic field magnitude to be varied without changing the shape shown in Figure 6; i.e. the B-field topology was constant as discussed in Section III A. The magnetization or BH curve of a material is a relation between the magnetic intensity ($\vec{H}$) and the magnetic induction or field ($\vec{B}$), which are related by the permeability (μ). The BH curve is material specific and can saturate causing distortions in the applied B-field of the HET. The H6 consists of iron pole pieces with carefully selected BH curves that begin to saturate above approximately 5.5 A of coil current, which set the upper bound of magnetic field testing at I_{IM} = 5.50, I_{OM} = 4.92 A or $B_r/B_r^*=B_r/B_r^*|_{max}=1.48$. Magnetic field sweeps were typically started from $B_r/B_r^*|_{max}$ and decreased until the thruster discharge was unstable. However, a 300-V sweep was conducted starting from $B_r/B_r^*|_{max}$ decreasing until thruster instability and then increased again returning to $B_r/B_r^*|_{max}$ in order to demonstrate directionality independence and the absence of hysteresis. The thruster was operated for approximately 3-5 minutes at each B_r/B_r^* setting during a sweep. In order to ensure thermal equilibrium, the thruster was operated for a minimum of 3 hours before conducting B-field sweeps and when changing conditions (discharge voltage or flow rates) was operated for 0.5 to 1 hour prior to sweeps. All flow rates at 300 V discharge voltage were repeated during different pump downs where the thruster was exposed to atmosphere between tests. Tests were also repeated with and without the probes shown in Figure 9 present in order to ensure the probes were not significantly altering the thruster operation.

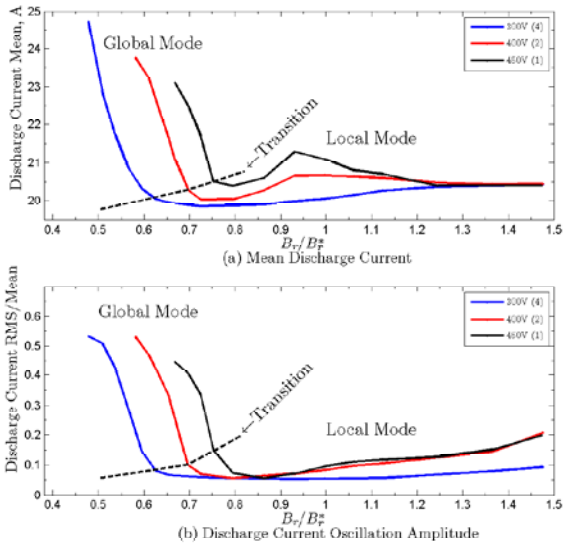

Figure 12. Discharge current mean (a) and oscillation amplitude (b) variation with constant 19.5 mg/s anode flow rate and variable discharge voltages of 300, 400 and 450 V. The number in parenthesis is the number of sweeps averaged together.

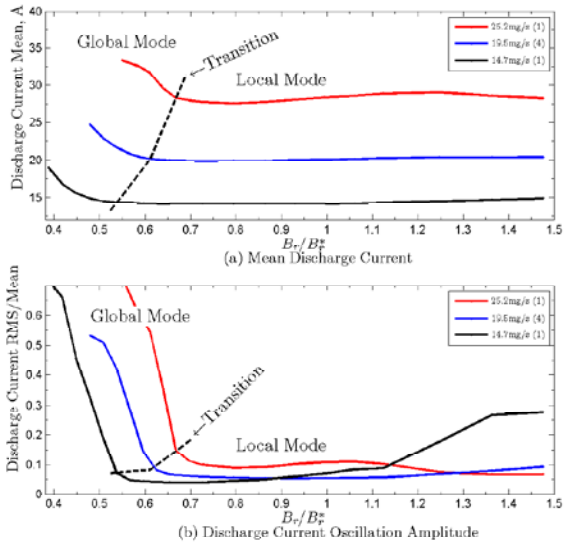

Figure 13. Discharge current mean (a) and oscillation amplitude (b) variation with constant 300 V discharge and variable anode flow rates of 25.2, 19.5 and 14.7 mg/s. The number in parenthesis is the number of sweeps averaged together.

Decreasing B_r/B_r^* below a certain threshold was shown to repeatedly induce a mode transition similar to those discussed in Section II where the mean discharge current increased and the discharge current amplitude increased. This was shown consistently for the three different voltages (300, 400 and 450 V) and three different flow rates (14.7, 19.5 and 25.2 mg/s) as shown in Figure 12 and Figure 13 where the plots of $\overline{I}_D$ and $\tilde{I}_D / \overline{I}_D$ vs. B_r/B_r^* show two distinct regions with a transition line. The thruster is considered to be more sensitive to mode transitions if the transition $B_r/B_r^*|_{trans}$ occurs at higher B_r/B_r^* values. Because $B_r/B_r^*|_{max}$ is an upper limit due to material properties inherent with the thruster design, if the transition point occurs at higher B_r/B_r^* then the range of B-field values where the thruster operates in local mode is diminished. As will be shown later, defining a single transition value for the B-field is misleading because there is a transition region where the plasma exhibits both types of oscillations,

however the transition typically occurred over only~10% change in B_r/B_r^*. The transition line shown is where global oscillation behavior begins to dominate and the transition region typically extends from 0.9 $B_r/B_r^*|_{trans}$ to $B_r/B_r^*|_{trans}$.

Figure 12 and Figure 13 show that increasing discharge voltage or flow rate makes the thruster more sensitive to mode transitions. The transition points from Figure 12 and Figure 13 have been summarized in Figure 14 in order to highlight the trends. Figure 12 (a) and (b) show the discharge current mean and oscillation amplitude, respectively, for discharge voltages of 300, 400 and 450 V. The parenthetical numbers in the legend show the number of sweeps where the 300-V condition was repeated four times (one sweep was a continuous decreasing then increasing sweep and one sweep was with probes) and the 400-V condition was repeated twice (once with probes and once without). The different sweeps showed remarkable consistency with deviations less than 3% of the mean indicating the transitions were not caused by transient thruster properties such as out-gassing or thermal dis-equilibrium.

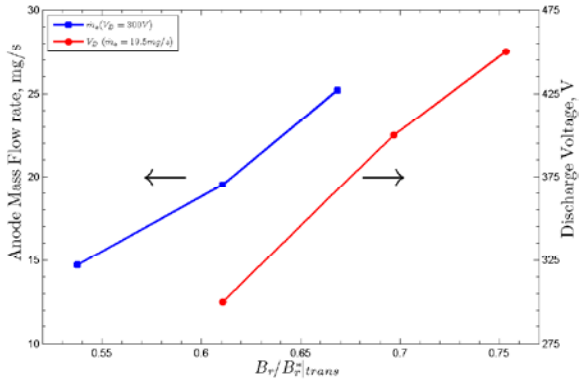

Figure 14. Mode transition point as a function of anode flow rate (left axis) at constant discharge voltage (300 V) and a function of discharge voltage (right axis) at constant anode flow rate (19.5 mg/s). The uncertainty in $B_r/B_r^*|_{trans}$ is ±0.03 and the transition region (not shown) is typically 0.06 starting at $B_r/B_r^*|_{trans}$ and decreasing.

Figure 13 and Figure 14 show that increasing anode flow rate with a constant 7% CFF makes the thruster more sensitive to mode transitions. Figure 13 (a) and (b) show the discharge current mean and oscillation amplitude, respectively, for anode flow rates of 14.7, 19.5 and 25.2 mg/s. Only 1 sweep at 14.7 mg/s is shown, although a second was conducted before all current sensors were calibrated and it yielded identical results. A second sweep at 25.2 mg/s was also conducted and not shown where the thruster was not operated at that flow rate for adequate time to reach thermal equilibrium, which caused a shift in mode transition. After adequate equilibrium time, the transition region stabilized. The higher discharge voltages of 400 V and 450 V in Figure 12 showed a steadily increasing oscillation amplitude as B_r/B_r^* was increased for $B_r/B_r^* \geq 1$, yet the mean discharge current remained the same. Additionally, the lowest flow rate case of 14.7 mg/s for 300 V showed significantly higher oscillation amplitude in Figure 13 for $B_r/B_r^* > 1.2$ than the other flow rates indicating a possible transition to an entirely different mode than the transition between global and local mode at B_r/B_r^* = 0.53. The estimated uncertainty in transition point is ±0.1 A for I_{IM} which corresponds to ±0.03 for $B_r/B_r^*|_{trans}$.

A distinction needs to be drawn between oscillatory operation in global mode and unstable operation. An increase in mean discharge current and oscillation amplitude is often labeled as unstable operation; however the thruster shows no sign of run-away behavior. Here we define unstable operation as the condition where discharge current begins to rise uncontrollably at a constant B-field setting. Figure 15 shows a typical B-field sweep at 300 V, 19.5 mg/s, lasting less than 1 hour with

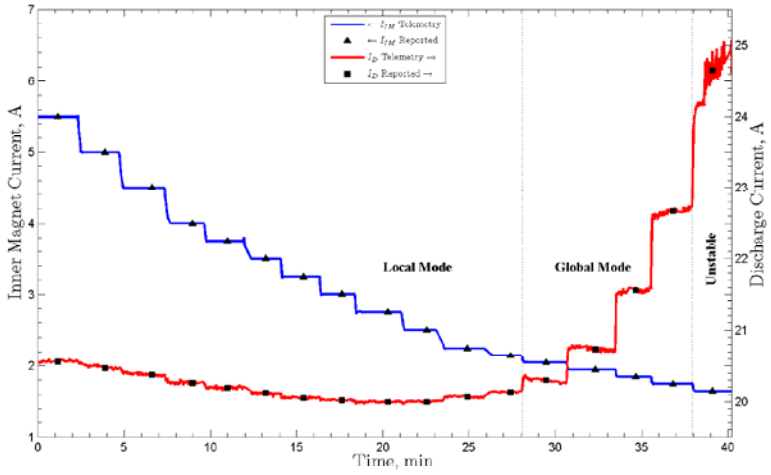

Figure 15. Telemetry for discharge current (right axis) and inner magnet current (left axis) for a B-field sweep at 300 V, 19.5 mg/s recorded at 1 Hz. The reported values used in Figure 12(a) and Figure 13(a) are shown as symbols. The B_r/B_r^* regions of local mode, global mode and unstable operation are noted.

approximately 3 minutes at each setting. The continuously recorded values for inner magnet current I_{IM} and mean discharge current $\overline{I}_D$ are shown in Figure 15 with the discrete values used in later plots shown as symbols. Inner magnet current is decreased from the max of 5.5 A in discrete steps until the thruster goes unstable at 1.65 A. From 5.5 A until 2.1 A, the thruster is in local mode and transitions to global mode below 2.1 A. From 2.1 A to 1.75 A the thruster is more oscillatory in global mode, but is stable at higher mean discharge current values. Below 1.75 A, the discharge current begins to steadily rise and significant fluctuations are seen even on the 1-Hz telemetry in Figure 15 without any thruster setting changes, which is unstable operation.

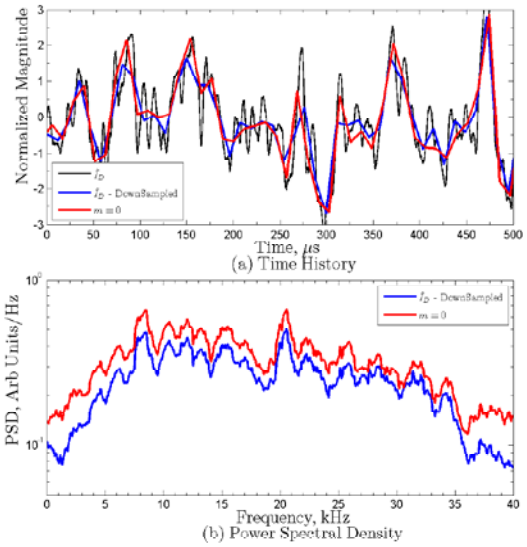

Figure 16. Comparison of normalized, AC component of the discharge current measurements to m=0 spoke order from FastCam analysis. (a) The time history of the discharge current signal shows higher frequency components than the m=0 signal, but the down-sampled discharge current and the m=0 signal are well correlated, ρ = 0.92. (b) PSD of the down sampled discharge current and m=0 signal also match well. A 1-kHz moving average filter has been applied to smooth both PSDs.

B. High-Speed Imaging and Spokes

FastCam videos of the thruster were acquired at all B_r/B_r^* settings during a B-field sweep and were time synchronized with discharge current measurements. All videos were processed as described in Section III A in order to generate a discharge current density surface as shown in Figure 11 (c). Figure 16 (a) compares a 0.5 ms sample of a $\hat{I}(t)$ signal and the $\hat{I}(t)$ signal filtered and down-sampled to the camera frame rate of 87.5 kHz with a normalized, AC component only m_0 from the FastCam. The native sample rate $\hat{I}(t)$ in Figure 16 (a) shows higher frequency discharge current oscillations that are not captured with FastCam. The difference between the $\hat{I}(t)$ signal and $\hat{I}(t)$ signal filtered and down-sampled yields the uncertainty $\sigma_{j_{D_b}3}(t)$ in Eq. (19). The correlation is visually apparent in Figure 16 (a) with a linear correlation coefficient of 0.92 between the down-sampled $\hat{I}(t)$ signal and m_0. This matches the result first reported by Lobbia.[34] A linear correlation coefficient of 0.8 or higher is always observed between I_D and m_0, supporting the assumption made in Section III A that the time varying light intensity within the discharge channel is linearly related to the discharge current. The PSD of the down-sampled $\hat{I}(t)$ and m_0 are nearly identical as shown in Figure 16 (b). Therefore, PSDs of the discharge current from the split core Hall probes and m_0 spoke order from HIA are excellent proxies for each other and are important comparisons during mode transitions.

During B-field sweeps, HIA of the discharge current density surface shows a distinct change in the discharge channel oscillations in Figure 17 where the transition point is B_r/B_r^* = 0.61. While in local mode (B_r/B_r^* > 0.61), the spoke surfaces in the right plots show clear diagonal stripes, indicative of strong, coherent spokes or azimuthally propagating perturbations. Figure 17 shows the discharge current mean and RMS values with HIA during the B-field sweep and mode transition for 300 V, 19.5 mg/s, where the nominal discharge current is 20 A or 133 mA/cm^2 average discharge current density.

Several important features can be distinguished on the discharge current density surface plots, beginning with the low magnetic field setting of B_r/B_r^* = 0.52. Vertical stripes of constant current density indicates the entire discharge channel is acting in unison with minimal azimuthal non-uniformities, as shown clearly in B_r/B_r^* = 0.52. The fluctuations are large with the entire discharge channel at 70 mA/cm^2 (10.6 A) or approximately half of the nominal value at the minima and then rising to over 300 mA/cm^2 (45 A) during the peak. In 1 ms of the discharge current density surface shown in Figure 17, 8.5 cycles are visible. This corresponds to a frequency of 8.5 kHz, which is clearly seen as a peak for m = 0 in the HIA PSD with corresponding harmonics at 17 and 25.5 kHz. The m = 1 spoke order peak is just an artifact from m = 0 which McDonald[32] describes as "smearing." No spokes are observed

to have any significant peaks for B_r/B_r^*= 0.52. The PSD peak in m_0 is over 10^7; 2 orders of magnitude higher than at the transition point (B_r/B_r^*= 0.61) or higher B_r/B_r^* values.

At the transition point, B_r/B_r^*= 0.61 in Figure 17, strong vertical stripes are seen between 0.46 and 0.73 ms as well as 0.9 ms, indicating an oscillation in the entire channel from 110 to 160 mA/cm^2. These entire channel oscillations are significantly lower than the global oscillations seen at B_r/B_r^*= 0.52. The three oscillations seen between 0.46 and 0.73 ms correspond to 11 kHz oscillations. However, diagonal stripes are clearly visible from 0 to 0.4 ms with oscillations between 120 to 150 mA/cm^2, which are symmetric about the mean of 133 mA/cm^2 for the discharge current of 20 A. These diagonal stripes represent azimuthal spokes propagating around the channel counter-clockwise, which is the E×B direction for the H6. The spokes extend for ¼ to ½ of the discharge channel before dissipating and last from 100 to 200 μs in duration. The existence of spokes and global channel oscillations simultaneously indicates the thruster is switching or "bouncing" between the different oscillatory modes. The PSD shows the magnitude of the global mode has decreased by 2 orders of magnitude and is now the 11 kHz noted above. Spoke orders m = 3-6 are present, with 4 and 5 the most dominant at 13 and 18 kHz, respectively.

For the nominal magnetic field of B_r/B_r^* = 1.00 in Figure 17, very few global oscillations are seen as evidenced by the very flat m_0 in the PSD and only hints of vertical lines in the spoke surface. Spoke orders m = 3-6 are also present with 4 and 5 still the most dominant, but they have shifted down to 10 and 15 kHz, respectively. The spokes are stronger as evidenced by the higher PSD peaks, but the length of the diagonal lines in the spoke surface has also increased. Spokes typically propagate over ½ to sometimes even the entire discharge channel lasting for several 100's μs. The local oscillations represented by spokes are from 115 to 150 mA/cm^2, which is about the mean of 133 mA/cm^2 or 20 A.

For the high magnetic field of B_r/B_r^*= 1.48 in Figure 17, the entire discharge channel occasionally oscillates in unison or "flickers" (i.e., 0.35 ms and 0.65 ms), but is not nearly as periodic as B_r/B_r^*= 0.52. The current density during these peaks can be as high as 180 mA/cm^2. Therefore, the m_0 mode is stronger than at B_r/B_r^*= 1.00, but the PSD peak is much broader than at B_r/B_r^*= 0.60 or 0.51 since the "flicker" is more sporadic and not at one frequency. The spoke orders m = 4-8 are nearly the same level, with 4 and 5 shifting down again to 9 and 14 kHz, respectively. The spoke peaks are an order of magnitude lower than B_r/B_r^*= 1.00 indicating weaker spokes. As seen qualitatively in the spoke surface, the spokes are shorter in duration so more spokes are present (higher spoke order) but propagate for shorter periods (lower PSD peaks).

In summary, B-fields below the transition thresholds do not support spoke propagation or local oscillations and the entire discharge channel oscillates in unison. At the transitions points, spokes are able to propagate but the channel occasionally reverts to global oscillation mode. At the nominal B-field strength spokes that are able to propagate over large regions of the discharge channel dominate and global oscillations are minimized. For higher B-field more spokes are present (higher m number in plots) but are less stable (occur for less time before disappearing in spoke surface). As B-field increases, the peak frequency of each spoke order decreases, which supports an inverse relation between the spoke frequency (i.e., spoke velocity) and B-field as noted in Ref. 14.

C. Probe Response

The two HDLP-ISR were positioned in front of the thruster at 6 o'clock for a B-field sweep at 400 V, 19.5 mg/s as shown in Figure 9 with the results shown in Figure 18. The mode transition occurs at B_r/B_r^* = 0.70, below which oscillation amplitude increases greatly. Unlike the 300-V case, for high B_r/B_r^* = 1.48 the oscillation amplitude $\tilde{I}_D$ is also quite large at 5 A or 25% of $\bar{I}_D$. The results reported below only use the ion saturation current signals from the ISR probes (I_{ISR}), although high-speed data were also collected from the HDLP. Simply looking at signal correlation and PSDs, the ISR signals are easier to use with less noise and uncertainty than the high-speed electron density, electron temperature or plasma potential results. The same scale factor of 10^5 used later in Figure 19 will be applied to the I_{ISR} signal before calculating PSDs in Figure 18 for a direct comparison to discharge current PSDs.

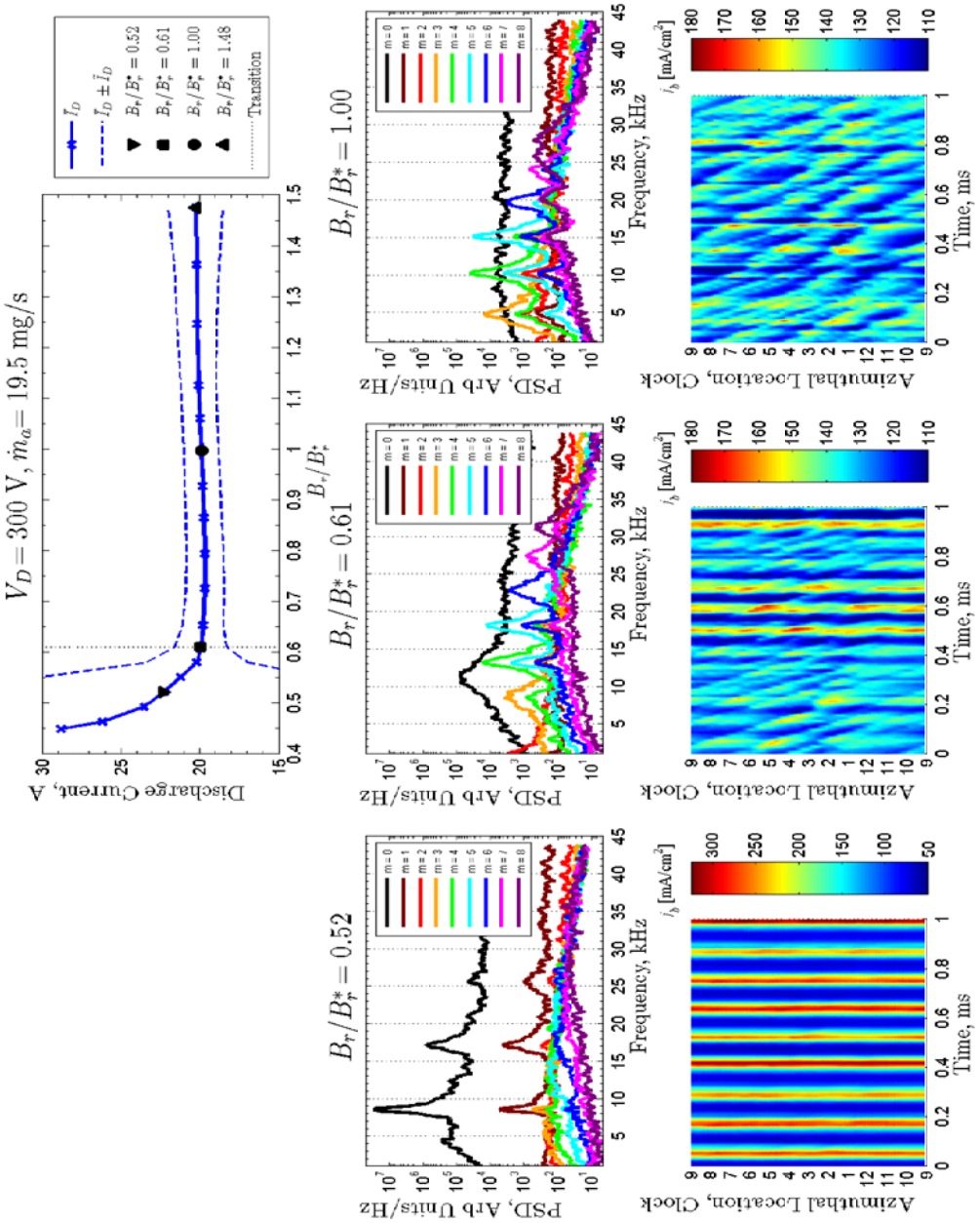

Figure 17. B-field sweep for 300 V, 19.5 mg/s showing transition at $B_r/B_r^* = 0.61$. The discharge current mean and oscillation amplitude are shown with the transition and for B_r/B_r^* settings selected for further analysis. The middle row plots are HIA PSDs and the bottom row plots are discharge current density. The scale range for $B_r/B_r^* = 0.52$ discharge current density is larger due to the magnitude of oscillations. A 500-Hz moving average filter has been applied to smooth all PSDs.

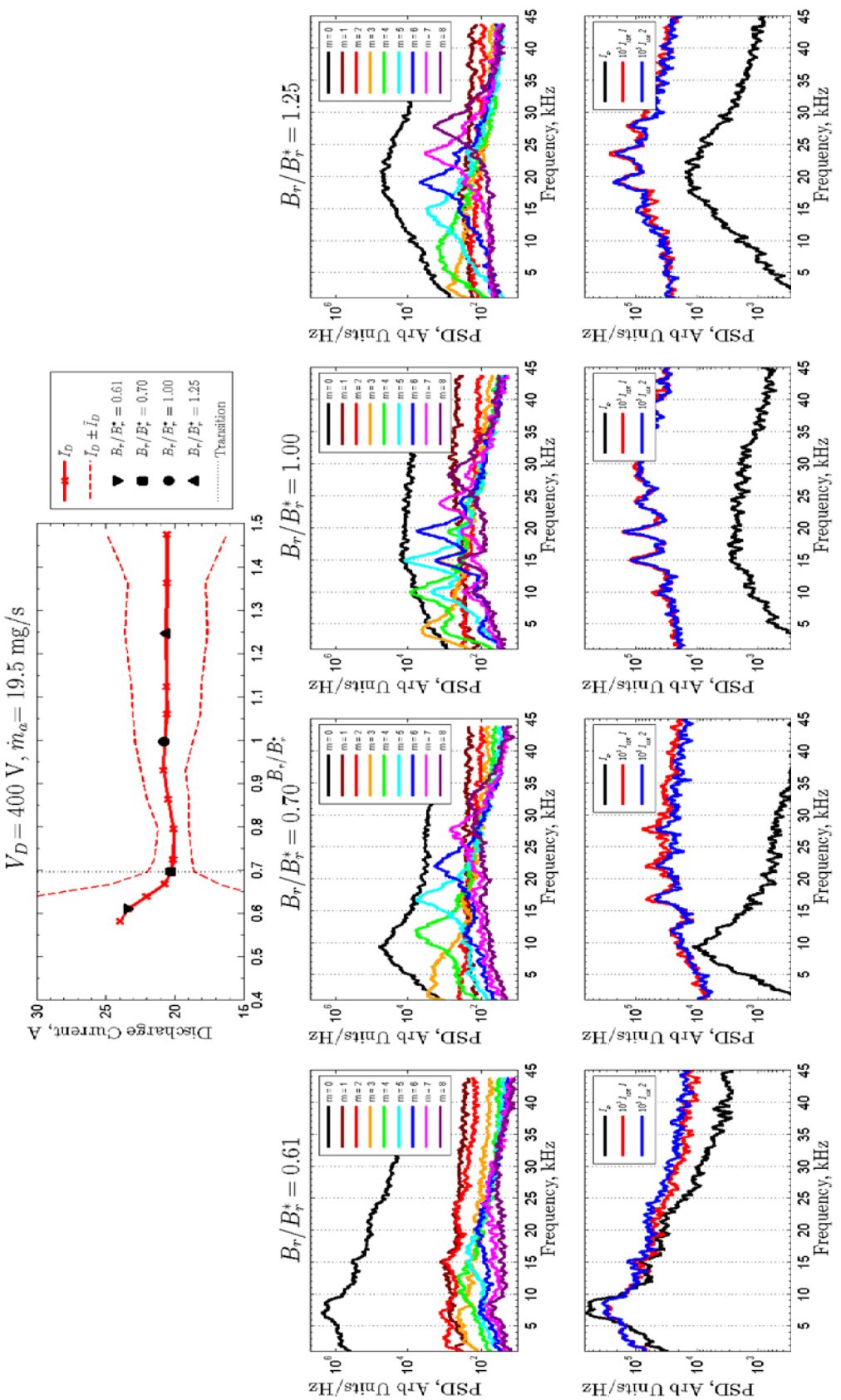

Figure 18. B-field sweep for 400 V, 19.5 mg/s with probes in place showing transition at $B_r/B_r^* = 0.69$. The discharge current mean and oscillation amplitude are shown with the transition and for B_r/B_r^* settings selected for further analysis. The middle row plots are HIA PSDs and the bottom row plots are discharge current and ISR signal PSDs. A-500 Hz moving average filter has been applied to smooth all PSDs.

For the global oscillation mode, $B_r/B_r^* = 0.61$, the discharge current and $m = 0$ PSDs have a flat peak between 6.6 to 8.5 kHz. This peak is over 1 order of magnitude larger than at $B_r/B_r^* = 0.70$ for $m = 0$ in the HIA PSD and almost 2 orders of magnitude larger for the discharge current. Both the HIA PSD and discharge current PSD are over two orders of magnitude larger than at $B_r/B_r^* = 1.00$. No spokes are present from HIA or the ISR signals. The discharge current signal peak is larger than the ISR signals, indicating the dominance of the global oscillations. At the transition point, $B_r/B_r^* = 0.70$, spokes are present with $m = 4$ and 5 dominant at 12 and 17 kHz, respectively. Spoke order $m = 6$ is present at 22 kHz and $m = 7$ order is present at 27 kHz one order of magnitude lower in signal strength than $m = 4$ or 5. The discharge current and $m = 0$ peaks have shifted to a sharp peak at 9 kHz. The ISR signals show the same peaks as the HIA spokes at 17, 22 and 27 kHz (the 12-kHz peak is weakly present), but the discharge current peak at 9 kHz is entirely absent. This shows local plasma oscillations due to spokes dominate over the global discharge current oscillations. The HIA spoke signals are an order of magnitude lower than the discharge current signal at $B_r/B_r^* = 0.70$, but the ISR signal is stronger than the discharge current.

At the nominal magnetic field, $B_r/B_r^* = 1.00$, the discharge current and $m = 0$ signals have a very broad peak between 15 and 20 kHz. On the HIA PSDs, the dominant spoke orders are $m = 3$, 4, 5 and 6 at 4, 10, 15 and 19 kHz, respectively, with the $m = 7$ order at 24 kHz and $m = 8$ order at 28 kHz also weakly present. The ISR signals have strong peaks at 15, 20 and 24 kHz matching the $m = 5$, 6 and 7 spoke orders well. There is also a broad signal starting at 28 kHz matching m = 8 and extending to 40 kHz which may be caused by the global discharge current. For a higher magnetic field, $B_r/B_r^* = 1.25$, the discharge current oscillations increase, as evidenced by a large (same magnitude as transition) and more peaked discharge current and $m = 0$ order at 20 kHz. On the HIA PSDs, the $m = 4$ spoke order has faded, but $m = 5$, 6, 7 and 8 have peaks at 15, 19, 24 and 28 kHz, respectively. The ISR signals show the same peaks with the strongest peaks at 19 and 24 kHz matching the $m = 6$ and 7 spoke orders. The peaks have shifted to lower frequencies, but by less than 0.5 kHz and all frequency peaks are rounded to the nearest kHz.

In summary, the PSDs for ISR 1 and 2 consistently match, indicating that they record the same plasma oscillations. This is important when doing the correlation later as it is shown they do not record the plasma oscillations at the same time. The ISR signal PSDs have peaks matching the HIA PSD peaks for spokes with the strongest peaks corresponding to the higher spoke orders. As with the 300-V case, the peak spoke orders *m* increase with increasing B_r/B_r^* but the frequency of the peaks gradually decreases. No spokes are present in global oscillation mode for ISR signals or HIA PSDs. As was hypothesized in Ref. 28, this indicates that in local oscillation mode, the plasma density fluctuations are determined by local oscillations within the discharge channel and not a global phenomenon. In global oscillation mode, the entire channel is oscillating in unison.

In order to further investigate local and global oscillations, a time history segment of the discharge current and ISR signals is shown in Figure 19 for local oscillation mode ($B_r/B_r^* = 0.73$) and global oscillation mode ($B_r/B_r^* = 0.61$). The ISR current (I_{ISR}) which is typically of order 100's μA and has been scaled by 10^5 with the mean subtracted (leaving the AC component only) in order to match the discharge current AC component $I_{D\,AC}$ for $B_r/B_r^* = 0.61$. The difference in the discharge current between the two modes in Figure 19(a) and (b) is also apparent with the local oscillation mode exhibiting lower mean and oscillation amplitude (RMS value) as shown in Table 2. The peak-to-peak value for the time segment shown in Figure 19(a) is less than 6 A for local mode, while the peak-to-peak value for the time segment shown in Figure 19(b) is ~35 A for global mode.

Table 2. Discharge current mean and oscillation amplitude for Figure 19.

	Local Mode	Global Mode
B_r / B_r^*	0.73	0.61
$\bar{I}_D$ [A]	20.1	23.4
$\tilde{I}_D$ [A]	1.4	11.0

For local oscillation mode, Figure 19(a), the linear correlation coefficient, ρ, between I_{ISR1} and $I_{D\,AC}$ is only 0.23, whereas in global oscillation mode, Figure 19(b) $\rho = 0.77$. This means I_{ISR1} tracks $I_{D\,AC}$ very well in global

oscillation mode, but not in local oscillation mode. In other words, the plasma oscillations in local oscillation mode are independent of the discharge current oscillations, but are not independent in global oscillation mode. The time delay calculated by cross-correlation from I_{ISR1} to I_{ISR2} is 14.7 μs, with an estimated uncertainty of ~1 μs based on the width of the correlation function or ~10% (1-2 μs) as discussed in Ref. 34. Figure 19(c) shows I_{ISR2} shifted to match I_{ISR1}, demonstrating the signals are very well correlated; the correlation coefficient before the time shift was -0.28 and after was 0.52. This means the ISR2 probe records the same plasma oscillations as ISR1, but delayed by 14.7 μs. The ISR2 probe signal delay is in the spoke propagation direction (E×B direction) from ISR1 leading to the conclusion that the plasma oscillations are caused by the passage of azimuthally propagating spokes as discussed in Ref. 28.

For global oscillation mode, Figure 19(b), the time delay calculated by cross-correlation from I_{ISR1} to I_{ISR2} was -1.4 μs, near the margin of error and the correlation coefficient ρ without time shifting was 0.75 so effectively there was no delay between ISR signals. However, the time delay calculated by cross-correlation from I_{ISR1} to $I_{D\,AC}$ was 9.7 μs, which can be construed as the ion time of flight from the discharge channel to the probes. This means the plasma oscillations occurred uniformly within the discharge channel during surges in discharge current and propagate downstream to be detected by both probes simultaneously.

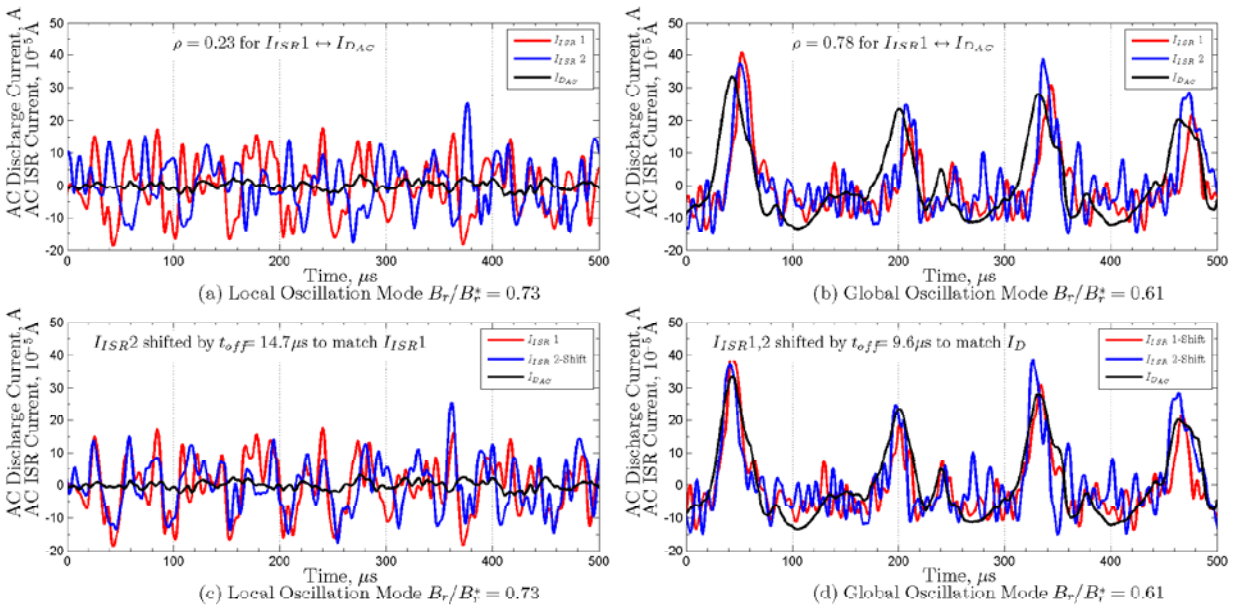

Figure 19. Comparison between the AC component of discharge current ($I_{D\,AC}$) to ISR current (I_{ISR1} and I_{ISR2}) for 400 V, 19.5 mg/s. Note the I_{ISR} signals have been scaled by 10^5, the I_{DAC} signals are true scale. The ISR signals were low-pass filtered at 150 kHz using a Butterworth 3rd order filter to reduce noise.

Key features identified in Figure 19 are time offsets from discharge current to ISR probes with correlation coefficients and time offsets between ISR probes. These quantities are shown in Figure 20 for 300 V and 400 V, 19.5 mg/s during B-field sweeps. Figure 20(a) shows the discharge current mean and oscillation amplitude with transition points during B-field sweeps, noting that 400 V transitions at a higher B_r/B_r^*. The correlation coefficients ρ in Figure 20(b) are between the AC components of I_{ISR1} and $I_{D\,AC}$ after time shifting I_{ISR1} by the offset times shown in Figure 20(d) calculated from cross-correlation. Figure 20(b) clearly shows for all B_r/B_r^* values in local oscillation mode, the ISR signal is not well correlated with the discharge current signal, as was shown in Figure 19. Below the transition value for B_r/B_r^* the signals become well correlated in global oscillation mode with $\rho > 0.3$. The offset time increases below the transition point for both 300 V and 400 V as shown in Figure 20(d) indicating a longer integrated ion time-of-flight from the discharge channel to the probes in global mode.

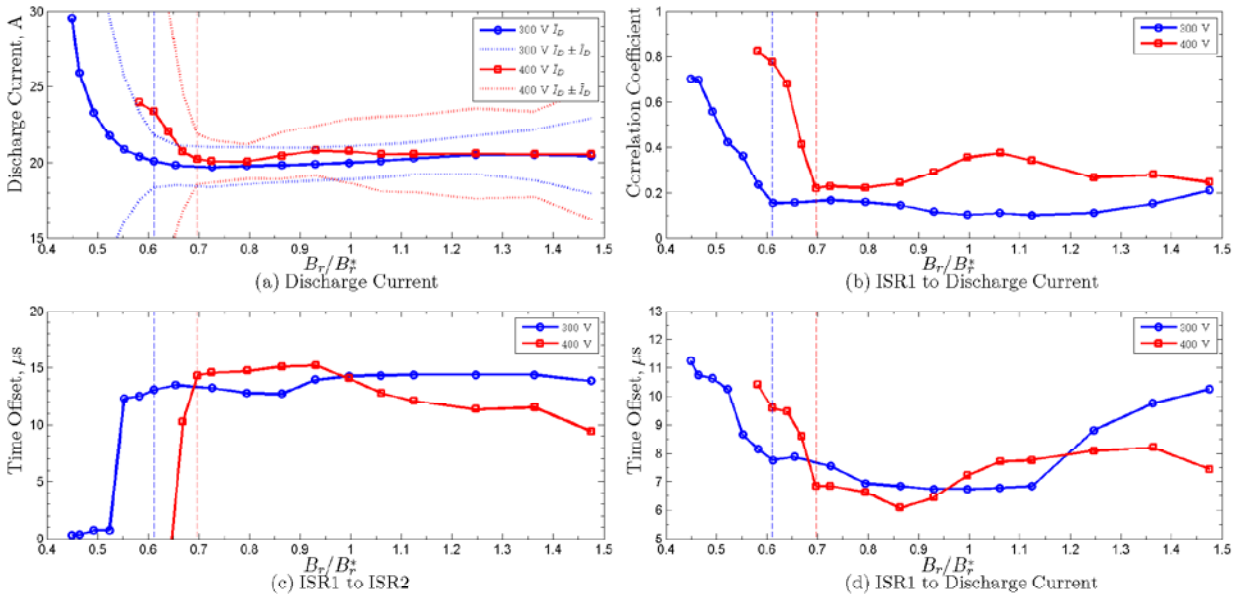

Figure 20. B-field sweeps at 19.5 mg/s for 300 V (blue) and 400 V (red) with ISR probes; transition points are shown as vertical dashed lines. (a) Discharge current mean values with oscillation amplitude in dotted lines. (b) Correlation coefficient from ISR1 to discharge current. (c) Time offset from ISR1 to ISR 2 calculated from cross-correlation (d) Time offset from ISR1 to discharge current calculated from cross-correlation.

The time offset from ISR1 to ISR2 calculated from cross-correlation is shown in Figure 20(c) where above the transition point the time delay is between 10 and 15 μs. The time delay is generally decreasing with increasing B_r/B_r^* for 400 V, but is relatively constant for 300 V. For both discharge voltages, below the transition point the offset time drops to within ±3 μs of 0 μs indicating the probes are measuring plasma oscillations nearly simultaneously. Combined with the high correlation coefficient between ISR1 and the discharge current, this indicates the plasma is oscillating in unison within the discharge channel and propagating downstream to be detected by the probes. For 300 V, the offset time does not immediately go near zero indicating some spoke propagation in the transition region of $B_r/B_r^* = 0.57$ to 0.61.

D. Thrust Measurements

Thrust was measured during B-field sweeps with the results for 300 V, 14.7 mg/s shown in Figure 21. The mean value for the thrust is 281 mN with a standard deviation of 3 mN, which is within the error of 7 mN or 2.5% of the mean value. Therefore, the thrust was constant within experimental error during the B-field sweep. The discharge current, however, increased below the transition point at $B_r/B_r^* = 0.54$ from 14 A to 19 A at $B_r/B_r^* = 0.39$. With a constant discharge voltage of 300 V, the increase in discharge current indicates an increase in power to the thruster so the thrust to power (T/P) decreases significantly in global oscillation mode. The peak T/P of 67 mN/kW occurs between $B_r/B_r^* = 0.64$ and 0.79 and decreases to 50 mN/kW at the minimum magnetic field, representing a 25% decrease in T/P.

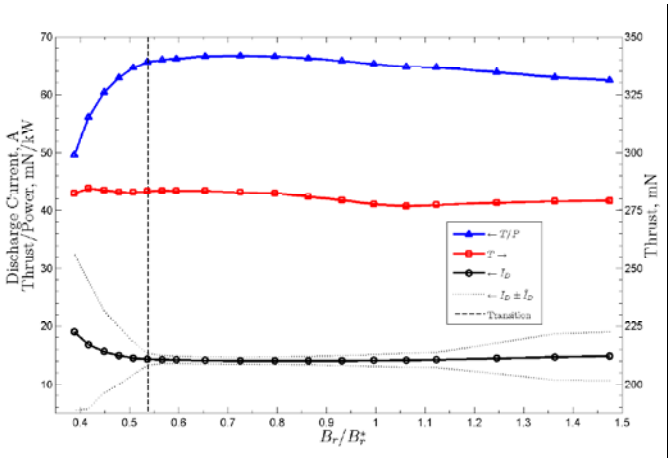

Figure 21. Thrust and T/P for 300 V, 14.7 mg/s during B-field sweep. The thrust is constant at 281 mN within experimental error, but the T/P decreases below the transition point as the discharge current increases.

E. Plume Photos

Digital photographs of the plume were taken from a view port at a nearly 90 degree angle with respect to thruster centerline. Photographs at different B_r/B_r^* settings in Figure 22 qualitatively show the plasma plume evolution during mode transitions. The viewing angle was slightly upstream so the discharge channel was visible very obliquely. The photos with accompanying contours were modeled after Figure 1 of Brown[13] which also qualitatively showed plume shape changes between modes. The contours show relative light intensity calculated from a grayscale version of the image where 1 is the brightest and 0 is dark. Note the probes can be seen as vertical lines of intensity ~0.2 in the plume at 1.5 channel radii downstream near the bottom of the picture and should be disregarded. Visible brightness is important because it indicates excited energy states caused by collisions. So although qualitative, the brightness of the plume is representative of the plasma physics occurring in the near-field region. Here we define the near-field plume region as the plasma directly downstream from the discharge channel to a few channel widths; the far-field plasma is the plasma outside of the near-field region.

In global oscillation mode where B_r/B_r^*= 0.46, the discharge channel is very bright with relative intensity 1 and the center spike of plasma extending along thruster centerline. The spike extends downstream over 1 channel diameter and dominates the plume. As B_r/B_r^* is increased to 0.61 at the transition point, the center spike recedes, but the discharge channel is still very bright at 1. At the nominal magnetic field setting, B_r/B_r^* = 1.0, where the thruster is in localized oscillation mode, the center spike is not present although the plasma from the cathode is still visible on centerline. The relative light intensity visible in the channel is only 0.6 to 0.7, which means the near-field plasma is less collisional and the collisions are likely occurring deeper within the channel where they are not visible to the camera. At B_r/B_r^* = 1.48, the discharge current oscillation amplitude is greater and the plume is again brighter downstream, but the channel relative brightness is still only 0.6 to 0.7. In general, the plume recedes as B_r/B_r^* is increased from global oscillation mode to local oscillation mode. This may indicate less collisions and other processes are occurring in the near-field plume and are more confined to within the discharge channel.

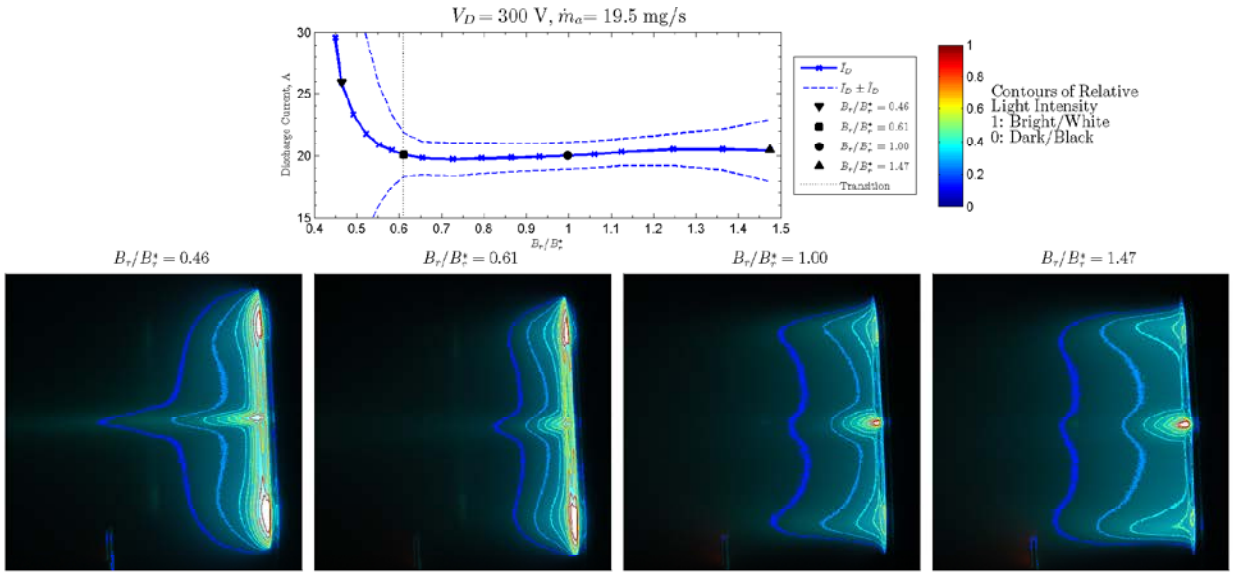

Figure 22. Plume photos showing light intensity during B-field sweep with the internal cathode at 300 V, 19.5 mg/s. Contours of relative intensity are shown to qualitatively illustrate the change in plume shape. Note the probes are present 1.5 channel radii downstream at the bottom and should be disregarded.

The same B-field sweep was conducted with the cathode mounted externally, as shown in Figure 23. For the low magnetic field setting, B_r/B_r^* = 0.48, the plume brightness extends downstream with the central spike dominating the plume structure. As B_r/B_r^* is increased to 0.57, the plume recedes towards the channel with some vestige of the center spike remaining. Both settings are in the global oscillation mode and the discharge channel relative brightness is 1. Increasing B_r/B_r^* above the transition point into local oscillation mode the center spike

disappears and the discharge channel relative brightness is only 0.6 to 0.7. The transition point for the external cathode case is higher B_r/B_r^* = 0.65 (not shown in Figure 23) than the internal case, where B_r/B_r^* = 0.61. The plume now extends out primarily along the channel indicating the plasma is well focused from the discharge channel downstream. Note the probes are present at the bottom and a reflection from the LVTF viewport sacrificial glass is visible as a vertical perturbation 1 channel radii downstream; both should be disregarded. For the external cathode case at 300 V, 19.5 mg/s, B_r/B_r^* was first swept from 1.48 to minimum and then increased again showing repeatability; the photos shown in Figure 23 are during the down sweep portion.

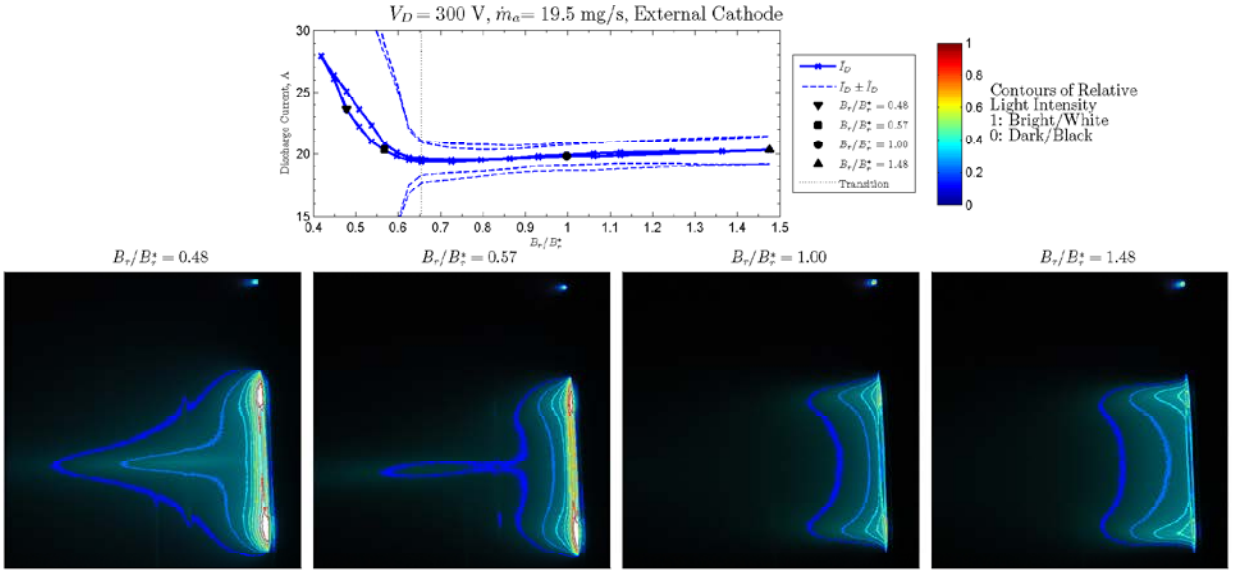

Figure 23. Plume photos showing light intensity during B-field sweep with the external cathode at 300 V, 19.5 mg/s. Contours of relative intensity are shown to qualitatively illustrate the change in plume shape. The probes are present at the bottom and a reflection from the LVTF viewport sacrificial glass is visible as a vertical perturbation 1 channel radii downstream, both should be disregarded. B_r/B_r^* was first swept from 1.48 to minimum and then increased again. The cathode is visible above the thruster at the 12 o'clock position.

VI. Discussion

The results shown above are significant in the description and definition of the commonly observed mode transitions. While the results do not answer the question of whether the mode transitions are wall-effect phenomena as stated by Gascon and Barral or a near-field plume effect as suggested by the work of Brown, they do provide valuable insight into HET operation.

A. Definitions of Modes

Here we define the modes by their plasma oscillation characteristics, where most conditions should be satisfied to represent either mode. An attempt is made to quantify the mode metrics, but the criteria values are meant only as a guide and not rigid discriminators. These criteria are based on the above observations of the H6 and are likely different for other HETs, but since mode transitions have been observed in other thrusters a subset of the criteria below should apply. These definitions delineate the thruster behavior when in either mode, but a less defined transition region exists between modes that typically extends from 0.9 $B_r/B_r^*|_{trans}$ to $B_r/B_r^*|_{trans}$. In this transition region, the thruster does not meet all of the criteria for either mode and the HIA clearly shows the thruster jumping between modes as evidenced from B_r/B_r^* = 0.61 in Figure 17.

Global Oscillation Mode The discharge current density in the entire channel is oscillating in unison with peak values of order 100% of the mean value and azimuthally propagating perturbations are either entirely absent or of negligible magnitude with respect to the discharge current density peaks. The m_0 mode of the HIA PSD has a clearly defined peak value and spoke orders $m > 1$ do not have peaks more than an order of magnitude above the

general noise floor. Azimuthally spaced probes do not observe delays in plasma property oscillations indicative of the entire channel luminosity or current density oscillating in unison, and are well correlated to the discharge current with $\rho > 0.3$. The discharge current oscillation amplitudes (RMS) are well above 10% of the mean discharge current value and the mean discharge current is over 15% higher than the minimum discharge current value obtained in a sweep. The discharge channel and near-field plume regions are observed to be brighter, indicative of increased collisions in the plume; a spike of bright plasma is visible on thruster centerline.

Local Oscillation Mode The discharge current density oscillations are dominated by localized perturbations that are less than 25% of the mean value and propagate in the E×B direction. Oscillations may be present where the entire channel luminosity or discharge current increases or decreases in unison, but they are sporadic and do not dominate the azimuthal propagations. The m_0 mode of the HIA PSD has a very broad peak value and spoke orders $m > 1$ have peaks more than an order of magnitude above the general noise floor. Azimuthally spaced probes observe clear delays in plasma property oscillations indicating localized regions of increased ionization within the discharge channel propagating downstream. The probe signals are not well correlated to the discharge current with $\rho < 0.3$. The discharge current oscillation amplitudes (RMS) are less than approximately 10% of the mean discharge current value and the mean discharge current is within 15% of the minimum discharge current value obtained in a sweep. The discharge channel and near-field plume regions are observed to be dimmer indicative of decreased collisions in the plume and collisional processes more confined to within the discharge channel. The plasma is well focused on discharge channel centerline and the center spike of plasma is absent for an external cathode or greatly diminished for an internal cathode.[‡]

B. Revisiting the Assumption of Linear Correlation between Local Light Intensity and Local Discharge Current Density

The ISR probes provide additional evidence that support the findings of Lobbia[34] where light intensity in the discharge channel is related to downstream density. From Eq. (7) the ion density is linearly related to the ISR current provided the electron temperature is constant. Therefore fluctuations in the ISR signal are indicative of oscillations in ion density, and through the quasi-neutral assumption, electron density as well. Note the relation in Eq. (7) is for thin-sheath Langmuir probe theory with only one ion species (+1) without a flowing plasma, but a HET plume by definition is a flowing plasma moving at approximately 20,000 m/s (well above the Bohm criteria[29]) and has multiple ion species. However, it is a reasonable assumption that the general relation between ISR current and ion density remain the same for the following discussion. In local oscillation mode, the PSD for segmented anodes, high-speed image analysis and ISR probes all show the same peaks. This indicates the same azimuthal or localized oscillations are detected by three separate, independent measurement techniques, however, this does not conclusively prove a linear correlation. In global oscillation mode, the time history and PSD for high-speed image analysis and ISR probes match showing a strong *linear* correlation.

Caution should be used in applying these techniques outside of discussions related to mode transitions or using these results to include or exclude different physical mechanisms for electron transport. While a correlation between light intensity, electron density and discharge current can be inferred from previous investigations and the present one, a linear correlation between local light intensity and discharge current density remains experimentally inconclusive. Regardless, the techniques used here are very helpful in describing the change in oscillatory behavior during mode transitions as they provide a clear means to discuss oscillation magnitude. The assumption of a linear relation between local light intensity and local discharge current density is rendered moot in global oscillation mode since the entire channel is oscillating in unison and the difference between local light intensity and global light intensity is negligible; i.e. for $B_r / B_r^* < B_r / B_r^*|_{trans}$ Eq. (6) and (14) are equal or $j_D(t) \cong j_{D_b}(b,t)$. The technique of calculating discharge current density adds significant value to describe the change in oscillatory behavior during mode transitions despite the lengthy assumption used in the derivation; e.g. in global oscillation mode the entire discharge channel current density fluctuates between 70 and 300 mA/cm^2 versus the local mode where the local oscillations are only ±20 mA/cm^2 from Figure 17.

[‡] An internal cathode will always produce a spike on thruster centerline because it is a plasma source.

C. Role of Spokes in Anomalous Electron Transport and Mode Transitions

The results from azimuthally spaced probes supports the ideas presented in Ref. 28 where rotating azimuthal non-uniformities (spokes) are azimuthally propagating regions of increased ionization producing a helical structure within the plasma. The regions of increased ionization propagating in the E×B direction would cause a delay between probe signals as illustrated in Figure 24. Spokes are dominant in local oscillation mode but absent in global oscillation mode where the probe signals show negligible time delay and are very well correlated to the discharge current. HIA also supports local versus global oscillations within the discharge channel. Extrapolating these results from the H6 to all annular HETs with similar magnetic field topologies such as the SPT-100, they should be operated in a mode where spokes are present because thruster performance in increased by decreasing discharge current.

As shown in Figure 21, thrust is constant but $\bar{I}_D$ increases, so extrapolating from Brown's work[13] the electron transport increases during transitions from local mode to global mode. The implication is that the presence of spokes indicates *decreased* electron transport to the anode. This raises an interesting causality question of whether the presence and mechanics of propagating spokes reduces electron transport to the anode or the plasma conditions that decrease electron transport also allow spokes to propagate. Regardless, the presence or disappearance of spokes is related to electron transport through the discharge channel to the anode and strong spoke behavior is a symptom of higher efficiency operation and should be sought after. Caution should be used when discussing electron transport as a global parameter when in actuality it will vary in different regions of the plasma with different effects on performance. As discussed in Ref. 3, electron transport in numerical models is often considered separately in different regions: near-plume, acceleration and near-anode. The near-field region mobility describes the ability for electrons to traverse through the plume from the cathode to supply electrons to the ionization zone which are critical for HET operation. The acceleration region mobility describes how well electrons are retained to undergo ionization collisions. The near-anode mobility describes the ability for electrons to reach the anode once they have escaped the acceleration/ionization region and influences the formation of the acceleration region. The combination of different electron mobility through the regions play a complex role in defining thruster stability and performance.

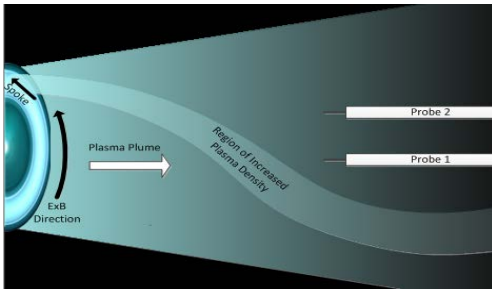

Figure 24. Illustration of spokes as regions of increased ion density producing helical structures of increased plasma density within the plume and how that would be measured by azimuthally spaced probes. Reproduced from Figure 12 of Ref. 28.

Spokes have been thought of as possible current carrying mechanisms to explain anomalous electron transport. Janes and Lowder[45] suggested that azimuthal electric fields from spokes could produce E×B drift in the axial direction and could account for anomalous electron transport. Recent work on a Cylindrical Hall Thruster (CHT)[46,47] has demonstrated that 50% of the discharge current is carried through a spoke (only one spoke is observed in the CHT). While CHT results have questionable relevance due to the significant difference in geometry (no inner channel wall) and magnetic field topology versus the H6, SPT-100 or any traditional annular discharge channel, they do reinforce the idea that significant current can pass through a spoke. Unfortunately, it was also reported that the CHT performance (measured by discharge current) increased when the spoke was *not* present,[48] which is opposite of what has been clearly shown in this work. Here electron transport decreases when spokes are present; based on these results, thrusters should be operated in local oscillation mode. Spokes cannot be the sole cause for anomalous electron transport because they are not present in global mode where electron transport is higher. Spokes are localized oscillations that are typically 10-20% of the mean discharge current density value while the global oscillation mode can be 100% of the mean value as shown in Figure 17. It is difficult to explain how a 10-20% oscillation can cause the order of magnitude higher electron transport than predicted by classical theory or Bohm diffusion[49]. A one-size fits all description for causes of anomalous electron transport is improbable and likely several different mechanisms are at work.

D. Ion Time-of-Flight and Ion Velocity

The specific impulse at the nominal conditions ($B_r/B_r^* = 1$) for the H6 at 300-V discharge is 1950 s,[15] which corresponds to an expected ion velocity of 19.1 km/s. From Figure 20 (d), the time offset at 300-V discharge for $0.8 < B_r/B_r^* < 1.1$ is approximately 7 μs. The corresponding ion velocity is 17 ±3 km/s using the fixed probe position 1.5 mean channel radii downstream and an uncertainty of ±1.5 μs in the time offset. Note that this is an average ion velocity in the region between the discharge channel exit plane and the probes and not an instantaneous velocity. In global oscillation mode the time offset is 10 μs which corresponds to an average ion velocity of 12 ±2 km/s. While both values are lower than expected, the nominal condition is within uncertainty of the expected ion velocity. As Lobbia points out, using linear cross-correlation to determine ion time-of-flight is less accurate than determining the phase delay from frequency domain transfer functions.[34] Therefore, the lower than expected average ion velocity may be the result of experimental uncertainty. It may also be indicative of changes in the plasma properties in global oscillation mode. The ion time-of flight from creation in the ionization zone to observation by ISR probes is calculated by integrating the ion position using the equation of motion for a particle in the axial electric field (assuming the ions are unmagnetized). The instantaneous ion velocity at the probes may be higher in global mode than the average ion velocity of 12 km/s calculated by simple ion time-of-flight, but the time for an ion to travel from the ionization zone to the probes may be longer due to a different plasma potential profile. Assuming conservation of energy, if the plasma potential at the probes is the same in global mode and local mode and if the ions are created at the same potential, then they should have the same instantaneous velocity. These subtleties mean that using the simple linear cross-correlation time offsets in Figure 20 (d) to calculate ion velocity can be misleading.

An example has been created using a measured plasma potential profile and an altered plasma potential profile to illustrate this hypothesis. The measured plasma potential profile with respect to the cathode has be extracted from Figure 15 of Ref. 15 and has been linearly extrapolated to the probe distance at $z/r = 1.5$ as shown in Figure 25. This is for the nominal H6 conditions which is local mode. A second plasma potential profile has been created by "stretching" the measured profile downstream, but the plasma potential at the probe location remains the same. This has been labeled as global mode in Figure 25 but does not represent a measured plasma potential profile. The equation of motion for a singly charged ion has been numerically integrated using energy conservation with distance increments of 1 μm to calculate the final velocity and total time of flight to reach the probes with the results shown in Figure 25. The calculated final ion velocities of 20.3 km/s are reasonable estimates of expected ion velocities from measurements and both time-of-flights fit with the data shown in Figure 20 (d). As expected, the final velocities are the same since they have been accelerated through the same potential, but the time of flight from $z/r = 0$ to $z/r = 1.5$ has increased by 2 μs for global mode to 10 μs. At present there are no direct measurements of plasma potential profile changes between local mode and global mode for the H6 and the global potential profile shown in Figure 25 is purely hypothetical. However, it does quantitatively demonstrate how the downstream probes could measure different time offsets and yield different average velocities when the ion instantaneous velocities are the same.

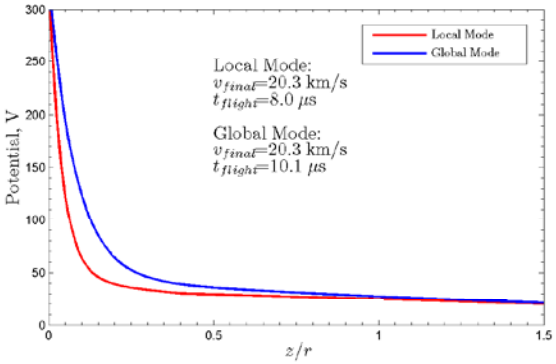

Figure 25. Plasma potential profiles with respect to ground to calculate ion time-of-flight. Local mode profile is based on measurements from Ref. 15. Global mode is based on a modified version of local mode for demonstrative purposes only. The calculated final velocity and time-of-flight are shown.

E. Plume Luminosity and Mode Transition Mechanisms

The photographs of Figure 22 and Figure 23 clearly show a change in light intensity in the near-field plume region after mode transition. Referencing optical emission characteristics for xenon,[50] neutral xenon dominates in the light blue to cyan portion of the visible spectrum (approximately 470 to 500 nm) with lines of 500+ intensity at

473, 481 and 492 nm. Xenon +1 ions dominate in the violet to blue portion of the spectrum (approximately 430 to 470 nm) with lines of 1000 intensity at 433 and 446 nm. Xenon +1 ions also have a strong 1000 intensity line at 508 nm in the cyan to green portion of the spectrum. Xenon +2 ions do not have any lines greater than 100 intensity in the 430 to 520 nm bandwidth. The human eye nor a standard digital camera are a calibrated spectrograph, but the plume is clearly blue in hue showing the combination of xenon neutral and +1 ions wavelengths. The blue hue of the plume extends outward (farther downstream) after the transition to global mode indicating that increased collisionality is occurring outside of the discharge channel. The luminosity is determined by collision rates (here we assume electron to neutral or electron to ion), which are functions of the particle densities (neutral, electron or +1 ions) and collision cross-sections (determined by electron temperature). Therefore, increased brightness after mode transition may indicate increased densities outside the channel or a change in electron temperature (increase or decrease depending on how cross section varies with electron temperature). If the increased luminosity are neutral lines (light blue to cyan), this may result from more neutral atoms escaping the discharge channel indicating the ionization zone is pushed out from the channel. If the ionization zone and plasma potential are pushed outside of the channel in global mode then the possibility exists that ions could be accelerated at nearly the discharge potential to very large incidence angles (up to ~90 degrees) from thruster centerline.

The question raised in Section II is whether wall effects or near-field plume properties were a cause for mode transitions. While this investigation does not conclusively answer this question, the presence or disappearance of spokes between modes may be an important clue. A possible explanation can be made from the wall-effect theory of Gascon and Barral[7,9] where the transition occurs when the discharge channel wall enters space charge saturation. As was discussed by King[51] based on single particle motion, a radial electric field at the outer wall is required to keep the electrons on a circular path in the discharge channel due to the cylindrical geometry. If the wall is in space charge saturation, then it may not be able to reflect the electrons back into the Hall current before they escape to the anode. This implies that the rotating spoke is caused by azimuthal motion of electrons in the Hall current and will be addressed in a future publication.

Not explicitly studied as a mode transition mechanism, another explanation should be considered where the so-called breathing mode oscillation is damped due to conditions within the discharge channel. The breathing mode is best described as a global depletion and replenishment of neutrals akin to the predator and prey models of ecosystems and is commonly observed in HET operation[52] and commonly accepted as a standard characteristic of HETs It has been qualitatively reproduced by numerical models [53,54] including a 1-D axial fluid simulation[55]. Changes in the B-field strength, neutral density or neutral replenishment of the ionization zone, ion residence time within the ionization zone (controlled by discharge potential) will all affect the breathing mode. A stability analysis, such as that started by Barral,[56,57] could show that mode transitions are a result of damping of the breathing mode. This will also be addressed in a future publication.

F. Thruster Performance

The 25% decrease in thrust-to-power during mode transition was similar to the results of the low voltage investigation of Brown.[13] The minimum mean discharge current typically occurred in local mode right before the transition region as shown in Figure 12 and Figure 13. Similarly, the peak *T/P* occurs near the transition point in Figure 21 where the thruster is on the verge of entering global oscillation mode. If one were to choose magnetic field settings for flight operation based on maximizing *T/P* or minimizing $\overline{I}_D$, then the thruster would be operating near the transition point where any perturbation in magnetic field (due to pole piece B-H properties changing over time, magnetic coils degrading, etc.) or changes in wall geometry and properties (due to erosion, coating from sputtered material, etc.) during the mission could cause the thruster to be more sensitive to transitioning from local oscillation mode to global oscillation mode. The B-field sweeps shown in Figure 12 and Figure 13 were constant and repeatable across several pump downs, but will likely change during the life of the thruster. This is more likely to be true if the transitions are related to wall effects where the plasma properties near the wall (i.e., susceptibility to space charge saturation) may change as the wall erodes. Therefore, discharge current versus B-field curves, while very repeatable during this test campaign, are likely only snapshots and may change after thousands of hours of

operation. The most important take-away from this investigation is a new perspective on performance mapping of thrusters. Figure 14 shows that the transition point occurs at higher B-field for increased anode flow rate or discharge voltage. Discharge current versus discharge voltage mapping (I_D-V_D) are commonly performed on thrusters at beginning of life or after thousands of hours of operation. However, more insight into thruster performance and stability margins is gained by also mapping B-field to generate or I_D-V_D-B maps for different flow rates and possibly even different facility background pressures. Using these results it can be assured that thrusters are not operated near a transition point where the thruster unintentionally enters global oscillation mode and decreases thruster performance.

VII. Conclusion

Previous researchers have identified mode transitions in HETs where a small change in a thruster operating parameter such as discharge voltage, magnetic field or mass flow rates causes the thruster discharge current mean and oscillation amplitude to increase significantly. Mode transitions in the H6 were induced by varying the magnetic field intensity while holding all other operating parameters constant and measurements were acquired with ion saturation probes and ultra-fast imaging. A technique that calculated discharge current density oscillations from FastCam images of the discharge channel was developed in order to quantify the fluctuations. Spokes are localized oscillations that are typically 10-20% of the mean discharge current density value, while the global oscillation mode can be 100% of the mean value.

The modes are described here as global oscillation mode and local oscillation mode. In global mode the entire discharge channel is oscillating in unison and spokes are either absent or negligible with discharge current oscillation amplitude (RMS) greater than 10% of the mean value. Downstream azimuthally spaced probes show no signal delay between each other and are very well correlated to the discharge current signal. In local oscillation mode perturbations in the discharge current density are seen to propagate in the E×B direction with clear spokes shown in a HIA PSD. The discharge current oscillation amplitude and mean values are significantly lower than global mode. Downstream azimuthally spaced probes show a clear signal delay between each other indicating the passage of spokes but are not well correlated to the discharge current indicating localized plasma oscillations within the discharge channel. The mode transitions were consistent across different tests and showed no hysteresis, but did change at different operating conditions. The transition between global mode and local mode occurred at higher relative B-field strengths for higher mass flow rate or higher discharge voltage. The results of this investigation do not conclude which mechanism, wall effects or near-field plume properties, were a cause for mode transitions.

The thrust was constant within experimental error through the mode transition but the thrust-to-power ratio decreased by 25% for the 14.7-mg/s flow rate; the peak in thrust-to-power occurs near the transition point. The plume showed significant differences between modes with the global mode significantly brighter in the channel and the near-field plasma as well as exhibiting a plasma spike on thruster centerline. For the external cathode case the plasma spike disappeared in local oscillation mode. Based on the research presented here, the H6 and likely any similar thruster should be operated in local oscillation mode to minimize discharge current and maximize performance. Thruster performance maps should include variation in discharge current, discharge voltage, B-field and flow rate to identify transition regions throughout the life of a thruster. Mode transitions provide valuable insight to thruster operation and suggest improved methods for thruster performance characterization.

Appendix

Start with the general equation for cross magnetic field velocity $v_{z\text{-}eff}$ for electrons in Cartesian coordinates[58] where z is the thruster axial direction. Neglect the $E_\theta \times B_r$ drift (which was addressed with Yoskikawa's[44] derivation) and diamagnetic drift

$$v_{z-eff} = -\mu_\perp E_z - \frac{D_\perp}{n_e}\frac{\partial n_e}{\partial z} \tag{26}$$

where E_z is the axial electric field, n_e is the electron density, the cross-field mobility $\mu_\perp$ and cross-field diffusion coefficient $D_\perp$ are defined as

$$\mu_\perp = \frac{\mu}{1+\omega_c^2/\nu_{eff}^2} \tag{27}$$

$$D_\perp = \frac{D}{1+\omega_c^2/\nu_{eff}^2} \tag{28}$$

The mobility coefficient μ and diffusion coefficient D have their usual meanings

$$D = \frac{eT_e}{m_e \nu_{eff}} \tag{29}$$

$$\mu = \frac{e}{m_e \nu_{eff}} \tag{30}$$

where the electron temperate T_e is in eV and the electron cyclotron frequency is $\omega_c = eB/m_e$. The effective collision frequency ν_{eff} can be broken down into electron-neutral collisions, electron-ion collisions, wall collisions and turbulence as discussed in Ref. 3. However, for this first order derivation only electron-neutral and electron-ion collisions will be considered. The generalized collision frequency for electrons with neutrals is[41]

$$\nu_{e-N} = k_m N \tag{31}$$

where N is the neutral density and k_m is a rate coefficient that is generally a function of electron temperature, but will be assumed as constant here. The collision frequency for electrons with +1 ions is[58]

$$\nu_{e-i} = \beta n_e$$
$$\beta = 2\times 10^{-12}\frac{\ln(\Lambda)}{T_e^{3/2}} \tag{32}$$

for T_e in eV and n_e in #/m^3 and $\ln(\Lambda) \cong 10$. The simplified effective collision frequency is

$$\nu_{eff} \cong k_m N + \beta n_e \tag{33}$$

Neglecting oscillations in electron temperature that change k_m and β, the effective collision frequency can be linearized as

$$\nu_{eff} = \bar{\nu}_{eff} + \tilde{\nu}_{eff} = k_m \bar{N} + k_m \tilde{N} + \beta \bar{n}_e + \beta \tilde{n}_e = \bar{\nu}_{eff} + k_m \tilde{N} + \beta \tilde{n}_e \tag{34}$$

The effective cross-field velocity from Eq. (26) must now be linearized by first combining Eqs. (26) through (30) and noting that $1/n_e\, \partial n_e/\partial z = \partial/\partial z \ln(n_e)$ so $v_{z\text{-}eff}$ can be written as

$$v_{z-eff} = -\frac{e}{m_e}\frac{\nu_{eff}}{\nu_{eff}^2+\omega_c^2}E_z - \frac{eT_e}{m_e}\frac{\nu_{eff}}{\nu_{eff}^2+\omega_c^2}\frac{\partial}{\partial z}\ln(n_e) \tag{35}$$

Linearizing Eq. (35) using (34) and neglecting oscillations in electric field and electron temperature, the effective cross-field velocity is

$$v_{z-eff} = -\frac{e}{m_e}E_z\left(\frac{\bar{\nu}_{eff}}{\bar{\nu}_{eff}^2+\omega_c^2} + \frac{\beta\tilde{n}_e}{\bar{\nu}_{eff}^2+\omega_c^2} + \frac{k_m\tilde{N}}{\bar{\nu}_{eff}^2+\omega_c^2}\right) - \frac{eT_e}{m_e}\left(\frac{\bar{\nu}_{eff}}{\bar{\nu}_{eff}^2+\omega_c^2} + \frac{\beta\tilde{n}_e}{\bar{\nu}_{eff}^2+\omega_c^2} + \frac{k_m\tilde{N}}{\bar{\nu}_{eff}^2+\omega_c^2}\right)\left(\frac{1}{\bar{n}_e}\frac{\partial\bar{n}_e}{\partial z} - \frac{\tilde{n}_e}{\bar{n}_e^2}\frac{\partial\bar{n}_e}{\partial z}\right) \tag{36}$$

where $\partial\tilde{n}/\partial z$ has been neglected and the assumption of $\tilde{n}/\bar{n} << 1$ has been used to justify a binomial expansion

$$\frac{\partial}{\partial z}\ln(\bar{n}_e+\tilde{n}_e) \sim \frac{1}{\bar{n}_e}\left(1-\frac{\tilde{n}_e}{\bar{n}_e}\right)\frac{\partial\bar{n}_e}{\partial z} \tag{37}$$

The assumptions in Eq. (36) while expanding the denominator include neglecting second order terms and assuming the oscillatory component in the denominator can be been neglected since $\bar{\nu}_{eff}^2+\omega_c^2 >> 2\bar{\nu}_{eff}\beta\tilde{n}_e + 2\bar{\nu}_{eff}k_m N$. The effective cross-field velocity $v_{z\text{-}eff}$ can now be written in the linearized form of steady $\bar{v}_{z-eff}$ and oscillatory $\tilde{v}_{z-eff}$ components

$$\bar{v}_{z-eff} = -\frac{e}{m_e}\frac{\bar{\nu}_{eff}}{\bar{\nu}_{eff}^2+\omega_c^2}E_z - \frac{eT_e}{m_e}\frac{\bar{\nu}_{eff}}{\bar{\nu}_{eff}^2+\omega_c^2}\frac{1}{\bar{n}_e}\frac{\partial\bar{n}_e}{\partial z} \tag{38}$$

$$\tilde{v}_{z-eff} = -\frac{\tilde{n}_e}{\bar{n}_e}\left[\frac{e}{m_e}\frac{\beta\bar{n}_e}{\bar{\nu}_{eff}^2+\omega_c^2}E_z + \frac{eT_e}{m_e}\frac{k_m\bar{N}}{\bar{\nu}_{eff}^2+\omega_c^2}\frac{1}{\bar{n}_e}\frac{\partial\bar{n}_e}{\partial z}\right] - \frac{\tilde{N}}{\bar{N}}\left[\frac{e}{m_e}\frac{k_m\bar{N}}{\bar{\nu}_{eff}^2+\omega_c^2}E_z + \frac{eT_e}{m_e}\frac{k_m\bar{N}}{\bar{\nu}_{eff}^2+\omega_c^2}\frac{1}{\bar{n}_e}\frac{\partial\bar{n}_e}{\partial z}\right] \quad (39)$$

Eq. (39) shows that given the lengthy list of assumptions and simplifications used above, the oscillatory component of the cross-field velocity is linearly related to electron and neutral density oscillations.

Table 3. Sample H6 properties used to calculate cross-field current density.

Variable	Value	Source
$\bar{n}_e$	2×10^{18} #/m^3	Figure 7-10 for 20 mg/s from Ref. 16, assumed from $\bar{n}_i$
N	2×10^{19} #/m^3	Figure 3-12 from Ref. 16 (simulation)
E_z	40 V/mm	Figure 7-21 for 20 mg/s from Ref. 16
T_e	30 eV	Figure 7-14 for 20 mg/s from Ref. 16, Figure 15 from Ref. 15
$\partial\bar{n}_e/\partial z$	10^{20} #/m^3/m	Figure 7-10 for 20 mg/s from Ref. 16, estimated from change in from $\bar{n}_i$ over ~L_{chnl}/2. Positive (directed downstream) for $z < L_{chnl}$, negative (directed upstream) for $z > L_{chnl}$.
k_m	2.5×10^{-13} m^3/s	From Ref. [55]

In order to validate this approach, sample values for the H6 can be used to calculate steady state current density, j, by inserting Eq. (38) in Eq. (22) to ensure the correct order of magnitude is obtained. Table 3 contains representative discharge channel plasma properties for the H6. The calculated current density is 155 mA/cm^2 where 149 mA/cm^2 is from the axial electric field with electron mobility term (first term in Eq. (38)) and 6 mA/cm^2 is from the electron density gradient with diffusion coefficient term (second term in Eq. (38)). Although the sign of $\partial\bar{n}_e/\partial z$ is dependent on location ($\partial\bar{n}_e/\partial z > 0$ for $z < L_{chnl}$ and $\partial\bar{n}_e/\partial z < 0$ for $z > L_{chnl}$), the difference is negligible since the gradient term is less than 4% of the discharge current density. This result is the correct order of magnitude for discharge current density which is ~130 mA/cm^2 at nominal conditions. Assuming small oscillations in electron and neutral densities, $\tilde{n}_e/\bar{n}_e \sim \tilde{N}/\bar{N} \sim 0.05$, using Eqs. (38) and (39) in Eq. (23) with the values in Table 3 yields an oscillation amplitude of ±15 mA/cm^2 which is ~10% of the mean value. This simple model calculates the correct order of magnitude steady state current density and yields reasonable oscillation amplitude, so it supports the idea that oscillations in density are linearly related to discharge current oscillations.

Acknowledgments

The primary author acknowledges this work was supported by a NASA Office of the Chief Technologist's Space Technology Research Fellowship (NSTRF). This work was also supported by AFOSR and AFRL through the MACEEP center of excellence grant number FA9550-09-1-0695. Dr. Mitat Birkan of AFOSR (and author Dr. Daniel Brown) is the MACEEP program manager. A portion of this research was carried out at the Jet Propulsion Laboratory, California Institute of Technology, under a contract with the National Aeronautics and Space Administration. The authors would like to thank two former PEPL students: Dr. Robert Lobbia for development of the HDLP; and Dr. Michael McDonald for development of the FastCam Analysis and many fruitful discussions. The author would also like to thank Dr. Benjamin Jörns of NASA JPL for insightful discussions and careful review of ideas as well as Marcel Georgin for the magnetic field simulations.

References

[1] Morozov, A. I., "The conceptual development of stationary plasma thrusters," *Plasma Physics Reports*, vol. 29, Mar. 2003, pp. 235–250.

[2] Morozov, A. I., Esipchuk, Y., Tilinin, G. N., Trofimov, A. V., Sharov, Y. A., and Shchepkin, G. Y., "Plasma accelerator with closed electron drift and extended acceleration zone," *Soviet Physics-Technical Physics*, vol. 17, Jul. 1972, pp. 38–44.

[3] Hofer, R., Katz, I., Mikellides, I., Goebel, D., Jameson, K., Sullivan, R., and Johnson, L., "Efficacy of Electron Mobility Models in Hybrid-PIC Hall Thruster Simulations," Hartford, CT: 2008.
[4] Mikellides, I. G., Katz, I., Hofer, R. R., and Goebel, D. M., "Magnetic shielding of walls from the unmagnetized ion beam in a Hall thruster," *Applied Physics Letters*, vol. 102, 2013, p. 023509.
[5] Tilinin, G. N., "High-frequency plasma waves in a Hall accelerator with an extended acceleration zone," *Soviet Physics-Technical Physics*, Aug. 1977.
[6] Yamamoto, N., Nakagawa, T., Komurasaki, K., and Arakawa, Y., "Influence of Discharge Oscillation on Hall Thruster Performance," Pasadena, CA: 2001.
[7] Gascon, N., Dudeck, M., and Barral, S., "Wall material effects in stationary plasma thrusters. I. Parametric studies of an SPT-100," *Physics of Plasmas*, vol. 10, 2003, p. 4123.
[8] Gascon, N., Meezan, N., and Cappelli, M., "Low Frequency Plasma Wave Dispersion and Propagation in Hall Thrusters," Pasadena, CA: 2001.
[9] Barral, S., Makowski, K., Peradzyński, Z., Gascon, N., and Dudeck, M., "Wall material effects in stationary plasma thrusters. II. Near-wall and in-wall conductivity," *Physics of Plasmas*, vol. 10, 2003, p. 4137.
[10] Baitin, A. V., Elizarov, L. I., Ivanov, A. A., and Bacal, M., "Maximum value and stability of near-wall current," Moscow, Russia: 1995.
[11] Jolivet, L., and Roussel, J.-F., "Effects of the secondary electron emission on the sheath phenomenon in a Hall thruster," Cannes, France: 2000.
[12] Mitrofanova, O. A., Gnizdor, R. Y., Murashko, V. M., Koryakin, A. I., and Nesterenko, A. N., "New Generation of SPT-100," Wiesbaden, Germany: 2011.
[13] Brown, D., and Gallimore, A., "Investigation of Low Discharge Current Voltage Hall Thruster Operating Modes and Ionization Processes," Ann Arbor, MI: 2009.
[14] McDonald, M., and Gallimore, A., "Parametric Investigation of the Rotating Spoke Instability in Hall Thrusters," Wiesbaden, Germany: 2011.
[15] Hofer, R., Goebel, D., Mikellides, I., and Katz, I., "Design of a Laboratory Hall Thruster with Magnetically Shielded Channel Walls, Phase II: Experiments," Atlanta, GA: 2012.
[16] Reid, B. M., "The Influence of Neutral Flow Rate in the Operation of Hall Thrusters," Ph.D. Dissertation, University of Michigan, 2009.
[17] Brown, D. L., "Investigation of Low Discharge Voltage Hall Thruster Characteristics and Evaluation of Loss Mechanisms," Ph.D. Dissertation, University of Michigan, 2009.
[18] Jameson, K. K., "Investigation of hollow cathode effects on total thruster efficiency in a 6 kW Hall thruster," Ph.D. Dissertation, University of California, Los Angeles, 2008.
[19] Shastry, R., "Experimental Characterization of the Near-Wall Region in Hall Thrusters and its Implications on Performance and Lifetime," Ph.D. Dissertation, University of Michigan, 2011.
[20] McDonald, M., "Electron Transport in Hall Thrusters," Ph.D. Dissertation, University of Michigan, 2012.
[21] Huang, W., "Study of Hall Thruster Discharge Channel Wall Erosion via Optical Diagnostics," Ph.D. Dissertation, University of Michigan, 2011.
[22] Hofer, R., Mikellides, I., Katz, I., and Goebel, D., "Wall Sheath and Electron Mobility Modeling in Hybrid-PIC Hall Thruster Simulations," Cincinnati, OH: 2007.
[23] Mikellides, I., Katz, I., Hofer, R., and Goebel, D., "Hall-Effect Thruster Simulations with 2-D Electron Transport and Hydrodynamics Ions," Ann Arbor, MI: 2009.
[24] Haag, T. W., "Thrust stand for high-power electric propulsion devices," *Review of Scientific Instruments*, vol. 62, 1991, p. 1186.
[25] Xu, K. G., and Walker, M. L. R., "High-power, null-type, inverted pendulum thrust stand," *Review of Scientific Instruments*, vol. 80, 2009, p. 055103.
[26] Lobbia, R., Sekerak, M., Liang, R., and Gallimore, A., "High-speed Dual Langmuir Probe Measurements of the Plasma Properties and EEDFs in a HET Plume," Wiesbaden, Germany: 2011.
[27] Lobbia, R. B., and Gallimore, A. D., "High-speed dual Langmuir probe," *Review of Scientific Instruments*, vol. 81, 2010, p. 073503.
[28] Sekerak, M., McDonald, M., Hofer, R., and Gallimore, A., "Hall Thruster Plume Measurements from High-Speed Dual Langmuir Probes with Ion Saturation Reference," Big Sky, MT: 2013.
[29] Cherrington, B. E., "The use of electrostatic probes for plasma diagnostics - A review," *Plasma Chemistry and Plasma Processing*, vol. 2, Jun. 1982, pp. 113–140.
[30] Swift, J. D., and Schwar, M. J. R., *Electrical probes for plasma diagnostics*, London; New York: Iliffe Books; American Elsevier, 1969.

[31] Bendat, J. S., and Piersol, A. G., *Engineering applications of correlation and spectral analysis*, New York: Wiley, 1980.
[32] McDonald, M., Bellant, C., St Pierre, B., and Gallimore, A., "Measurement of Cross-Field Electron Current in a Hall Thruster Due to Rotating Spoke Instabilities," San Diego, CA: 2011.
[33] McDonald, M. S., and Gallimore, A. D., "Rotating Spoke Instabilities in Hall Thrusters," *IEEE Transactions on Plasma Science*, vol. 39, Nov. 2011, pp. 2952–2953.
[34] Lobbia, R., Liu, T., and Gallimore, A., "Correlating time-resolved optical and Langmuir probe measurements of Hall thruster dynamics," Orlando, FL: 2008.
[35] Bevington, P. R., and Robinson, D. K., *Data reduction and error analysis for the physical sciences*, New York: McGraw-Hill, 1992.
[36] *MATLAB R2012a*, Natick, MA: MathWorks, Inc., 2012.
[37] Strum, R. D., *First principles of discrete systems and digital signal processing*, Reading, Mass: Addison-Wesley, 1988.
[38] Oppenheim, A. V., *Discrete-time signal processing*, Englewood Cliffs, N.J: Prentice Hall, 1989.
[39] Griem, H. R., and Cambridge University Press, *Principles of Plasma Spectroscopy*, Cambridge: Cambridge University Press, 1997.
[40] Hutchinson, I. H., and Cambridge University Press, *Principles of Plasma Diagnostics*, Cambridge: Cambridge University Press, 2002.
[41] Lieberman, M. A., and Lichtenberg, A. J., *Principles of plasma discharges and materials processing*, Hoboken, N.J.: Wiley-Interscience, 2005.
[42] Goebel, D., and Katz, I., *Fundamentals of Electric Propulsion : Ion and Hall Thrusters*, Hoboken N.J.: Wiley, 2008.
[43] Cappelli, M., Meezan, N., and Gascon, N., "Transport Physics in Hall Plasma Thrusters," Reno, NV: 2002.
[44] Yoshikawa, S., and Rose, D. J., "Anomalous Diffusion of a Plasma across a Magnetic Field," *Physics of Fluids*, vol. 5, 1962, p. 334.
[45] Janes, G. S., and Lowder, R. S., "Anomalous Electron Diffusion and Ion Acceleration in a Low-Density Plasma," *Physics of Fluids*, vol. 9, 1966, p. 1115.
[46] Raitses, Y., Griswold, M., Ellison, L., Parker, J., and Fisch, N., "Studies of Rotating Spoke Oscillations in Cylindrical Hall Thrusters," Atlanta, GA: 2012.
[47] Ellison, C. L., Raitses, Y., and Fisch, N. J., "Cross-field electron transport induced by a rotating spoke in a cylindrical Hall thruster," *Physics of Plasmas*, vol. 19, 2012.
[48] Parker, J. B., Raitses, Y., and Fisch, N. J., "Transition in electron transport in a cylindrical Hall thruster," *Applied Physics Letters*, vol. 97, 2010, p. 091501.
[49] Garrigues, L., Pérez-Luna, J., Lo, J., Hagelaar, G. J. M., Boeuf, J. P., and Mazouffre, S., "Empirical electron cross-field mobility in a Hall effect thruster," *Applied Physics Letters*, vol. 95, 2009, p. 141501.
[50] Lide, D. R., *CRC Handbook of Chemistry and Physics.*, Boca Raton: CRC Press, 1992.
[51] King, L., "A (Re-)examination of Electron Motion in Hall Thruster Fields," Princeton University: 2005.
[52] Choueiri, E. Y., "Plasma oscillations in Hall thrusters," *Physics of Plasmas*, vol. 8, 2001, p. 1411.
[53] Boeuf, J. P., and Garrigues, L., "Low frequency oscillations in a stationary plasma thruster," *Journal of Applied Physics*, vol. 84, 1998, p. 3541.
[54] Fife, J., Martínez-Sánchez, M., and Szabo, J., "A Numerical Study of Low-Frequency Discharge Oscillations in Hall Thrusters," Seattle, WA: 1997.
[55] Barral, S., and Ahedo, E., "Low-frequency model of breathing oscillations in Hall discharges," *Physical Review E*, vol. 79, Apr. 2009.
[56] Barral, S., and Peradzynski, Z., "A new breath for the breathing mode," Ann Arbor, MI: 2009.
[57] Barral, S., and Peradzyński, Z., "Ionization oscillations in Hall accelerators," *Physics of Plasmas*, vol. 17, 2010.
[58] Chen, F. F., *Introduction to plasma physics and controlled fusion.*, New York: Plenum Press., 1990.